Report no.
UC SESM 76-5

STRUCTURAL ENGINEERING AND STRUCTURAL MECHANICS

A FINITE ELEMENT MODEL OF FLUID FLOW IN SYSTEMS OF DEFORMABLE FRACTURED ROCK

by

HANS M. HILBER
ROBERT L. TAYLOR

NOVEMBER 1976

DEPARTMENT OF CIVIL ENGINEERING
UNIVERSITY OF CALIFORNIA
BERKELEY, CALIFORNIA

Department of Civil Engineering
Division of Structural Engineering
and Structural Mechanics

Report No. 76-5

A FINITE ELEMENT MODEL OF FLUID FLOW IN SYSTEMS OF DEFORMABLE FRACTURED ROCK

by

Hans M. Hilber and Robert L. Taylor

Report to

National Science Foundation

University of California
Berkeley, California

November 1976

ABSTRACT

We introduce a two-dimensional finite element model of fluid flow in fractured rock masses wherein the discontinuities are deformable and constitute the primary flow paths. The interaction between the fluid and the fracture motions as well as inertia effects are taken into account. The model permits us to simulate fractured rock systems which are at an incipient state of instability; it is possible to predict the behavior of such systems when their state of stress is changed by injection or removal of fluid.

A computer program based on this theory has been developed. It determines the hydrodynamic state of the fluid, the displacement, strain and stress response histories of the rock masses, the change of the kinetic and the potential energy of the rock, and the amount of energy dissipated during slip. A number of simplified problems are solved. The results confirm that the present model can be used to study the controlled release of tectonic stresses along predetermined faults through fluid injection.

TABLE OF CONTENTS

ACKNOWLEDGEMENT

We would like to acknowledge the support for this work provided by the National Science Foundation under contract number GK-42776. We thank Ellen McKeon for typing and editing the manuscript.

1. INTRODUCTION

Considerable evidence, gathered recently at Rangely, Colorado oil field, strongly suggests that fluid injection has caused small earthquakes along a fault. This and similar observations are described by Dietrich, Raleigh and Bredehoeft [1] and Handin and Raleigh [3], among others. Consequently the concept was developed that if earthquakes can be made by man's injection of fluid into the subsurface, then perhaps the appropriate control of fluid pressures in the earth's crust can lead to a method of earthquake control along major faults [3]. In order to study the role of fluids in controlling the behavior of fractured rock masses, it is necessary to develop both mathematical models and corresponding computer programs that allow the engineer to simulate the behavior of such systems under a wide range of field conditions.

Recently several attempts at developing appropriate mathematical models have been reported [4-10]. Gale, Taylor, Witherspoon and Ayatollahi [8], modifying the two-dimensional finite element formulation described in [6,7], successfully simulated quasi-static processes in systems of deformable fractured rock wherein the discontinuities constitute the dominant flow paths. However, the dynamic nature of slip mechanisms limit the applicability of the quasi-static model to the study of pre-failure conditions. Dietrich et al. [1,2] developed a dynamic finite element model for a single fault that undergoes slip under the influence of tectonic and predetermined fluid stresses. This model is able to provide a basis for predicting the dependence of displacements and near field transient motions on stress drop, rupture dimensions and seismic energy. However, Dietrich's model was not designed to incorporate the interactive processes between the fluid pressure, the fracture deformations and the stresses in the rock.

Since it appeared that the commonly known computational models all are unnecessarily restricted, an effort was made to develop a more realistic model that could simulate transient interactive processes in systems of fluid flow in deformable fractured rock. Based on the two-dimensional formulation of Gale et al. [8] we have been able to create a new finite element model which accounts for the inertia effects in the rock and the coupling between the fluid flow and the motion of the system of fractures. The new model simulates quasi-static and dynamic processes, and can be used to study the effect of fluid injection into systems which are at an incipient state of instability. This report is devoted to a description of the theory and the nonstandard computational techniques of the new model.

We are directing our attention to idealized geological structures which consist of a deterministic system of fractures in a two-dimensional elastic body of rock. The fluid flow is assumed to be confined to the network of fractures. The discretization procedure employed in the present study is schematically illustrated in Figure 1. The geological structure consists of four continuous domains separated by two intersecting curvilinear fracture surfaces. In Figure 1, both the geological structure and the corresponding discrete model are shown. In the discrete model, the following three types of finite elements are identified: (a) an isoparametric quadrilateral element discretizing the continuous domains, (b) a four-node joint element modelling the fractures, and (c) the one-dimensional, two-node fluid flow element. The intersections of the fracture elements with each other and with the boundaries define the nodal points of the mesh formed by the fluid elements. Thus, the meshes defined by fracture elements and by fluid elements,

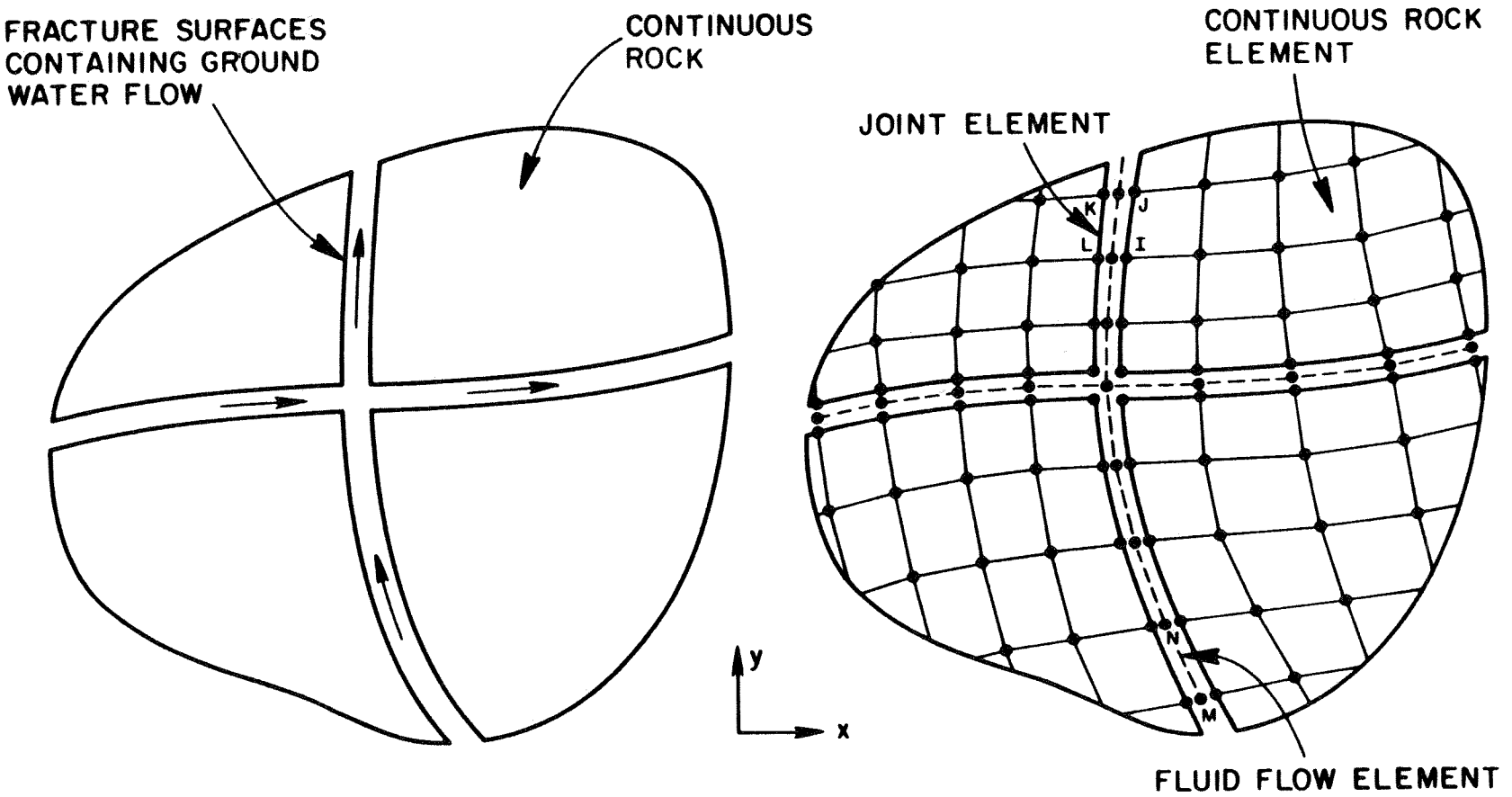

TYPICAL DETAIL OF A SYSTEM OF FRACTURED ROCK

FINITE ELEMENT MESH OF A SYSTEM OF FRACTURED ROCK

Fig. 1. Detail of an idealized two-dimensional region of a fractured rock system.

respectively, possess the same topological and geometrical data.

The behavior of the continuous rock mass is assumed to be described by the equations of linear elastodynamics. Effects due to the porosity of the rock are neglected. The finite element formulation of the elastic solid parts of the mesh is standard and will not be repeated here; for a detailed description of the relevant techniques the reader is referred to Zienkiewicz [12]. The nonstandard aspects of the discrete model will be addressed subsequently in Chapters 2, 3 and 4.

In Chapter 2 we outline the theory of the joint element and define the initial value problem which governs the dynamic behavior of the fractured rock masses. The opening, closing and slip mechanisms of the fracture surfaces are modeled by simplified contact and friction laws. Rate effects in the constitutive relations and failure criteria have not been included in the present model. Also the effects of shear dilitancy have been neglected in the constitutive relations of the joint element.

Chapter 3 is devoted to a description of the theory of fluid flow in the network of fractures. First we derive the flow element. It is based on a Galerkin formulation of a simplified Navier-Stokes equation. This formulation accounts for time dependent volumetric changes of the fluid due to fracture motions, and allows for nonuniform cross-sectional areas of the flow paths. Finally, we define and discuss the set of differential equations which determines the state of the fluid in the network of fractures.

The present finite element formulation of fluid flow in deformable fractured rock leads to two coupled systems of nonlinear differential equations. In Chapter 4 we outline the computational techniques and solution strategies which are employed in solving these equations. We

use standard step-by-step integration methods of structural dynamics to replace the differential equations by approximating algebraic equations of recursive form. Furthermore, we discuss suitable iterative techniques to solve these nonlinear equations in each time step.

Chapter 5 presents five applications of this finite element model to simplified problems in order to demonstrate some of its pertinent properties. Conclusions from this investigation are summarized in Chapter 6.

2. A KINEMATIC FINITE ELEMENT MODEL OF FRACTURED ROCK

In this chapter we define the initial value problem which approximately describes the dynamic behavior of systems of fractured rock. Particularly, we outline in detail the theory of the joint element which models contacting and frictional motions of fracture surfaces.

2.1 TANGENT FORMULATION OF THE JOINT ELEMENT

The geometry of a typical joint element located in the x,y plane is defined in Figure 2. The top and bottom faces of the joint element are kinematically constrained in the same way as the boundaries of adjacent continuous elements, insuring inter-element compatibility of displacements:

$$\begin{bmatrix} u_x \\ u_y \end{bmatrix}_B = \psi_1 \begin{bmatrix} u_x \\ u_y \end{bmatrix}_1 + \psi_2 \begin{bmatrix} u_x \\ u_y \end{bmatrix}_2 \quad , \tag{2.1a}$$

$$\begin{bmatrix} u_x \\ u_y \end{bmatrix}_T = \psi_1 \begin{bmatrix} u_x \\ u_y \end{bmatrix}_4 + \psi_2 \begin{bmatrix} u_x \\ u_y \end{bmatrix}_3 \quad , \tag{2.1b}$$

where u_x and u_y are displacements in x and y direction, respectively. In (2.1) subscript B stands for bottom face (nodes 1,2), subscript T stands for top face (nodes 3, 4), the vector $(u_x,u_y)_i^T$ contains the displacements u_x and u_y of node i, i = 1,2,3,4, and

$$\left.\begin{aligned} \psi_1 &= (1 - \xi)/2 \\ \psi_2 &= (1 + \xi)/2 \end{aligned}\right\} \tag{2.2}$$

are linear interpolation functions defined over the domain $-1 \leq \xi \leq 1$. Displacement components with respect to the local axes s, n are defined by the linear transformation

$$\begin{bmatrix} u_s \\ u_n \end{bmatrix} = \underset{\sim}{c} \begin{bmatrix} u_x \\ u_y \end{bmatrix} \quad , \tag{2.3a}$$

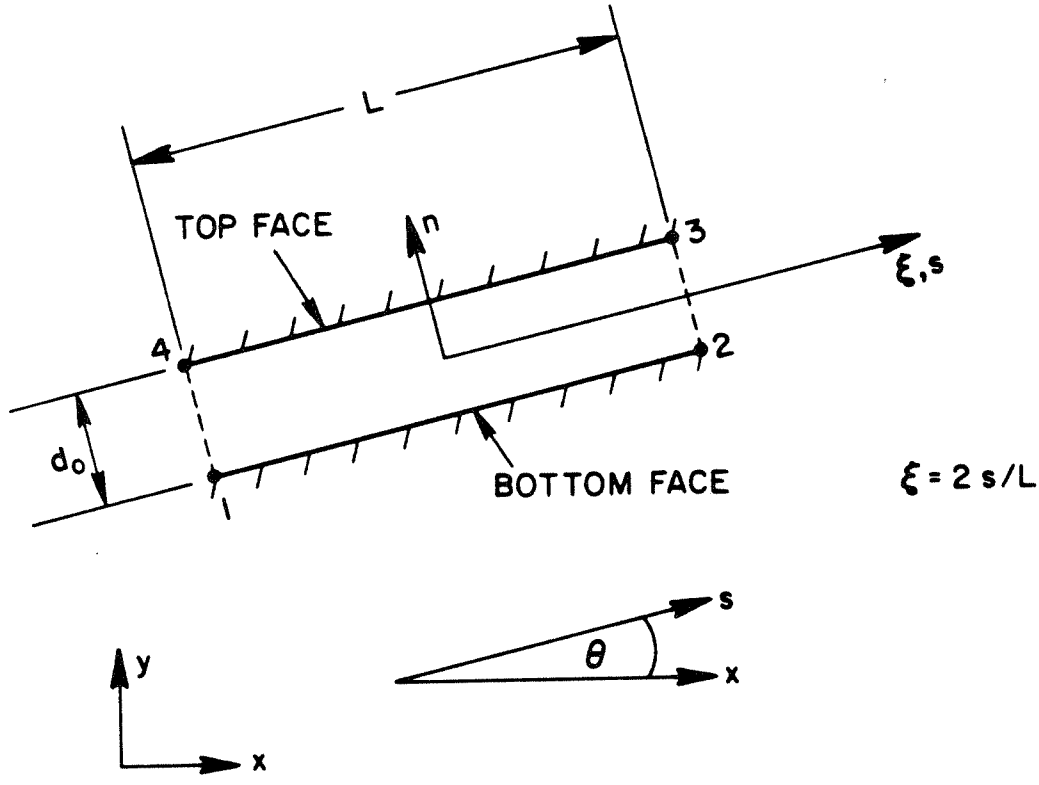

Fig. 2. Geometry and coordinate systems of the undeformed joint element.

where

$$\underset{\sim}{c} = \begin{bmatrix} \cos\Theta & \sin\Theta \\ -\sin\Theta & \cos\Theta \end{bmatrix} , \tag{2.3b}$$

$\cos\Theta = \Delta x/L$, $\sin\Theta = \Delta y/L$, $\Delta x = x_2 - x_1$, $\Delta y = y_2 - y_1$, $L = (\Delta x^2 + \Delta y^2)^{1/2}$, and u_s and u_n are the displacements in directions s and n, respectively; see Figure 2.

Shear and normal strains are defined by

$$\varepsilon_s = (u_s)_T - (u_s)_B \tag{2.4a}$$

and

$$\varepsilon_n = (u_n)_T - (u_n)_B \quad , \tag{2.4b}$$

respectively, which in view of (2.1) and (2.3) implies that

$$\left.\begin{aligned} \varepsilon_s &= \underset{\sim}{\phi}\, \underset{\sim}{\rho}_s \\ \varepsilon_n &= \underset{\sim}{\phi}\, \underset{\sim}{\rho}_n \end{aligned}\right\} . \tag{2.5}$$

In (2.5)

$$\underset{\sim}{\phi} = (-\psi_1, -\psi_2, \psi_2, \psi_1) \tag{2.6}$$

and

$$\left.\begin{aligned} \underset{\sim}{\rho}_s &= (u_{s1}, u_{s2}, u_{s3}, u_{s4})^T \\ \underset{\sim}{\rho}_n &= (u_{n1}, u_{n2}, u_{n3}, u_{n4})^T \end{aligned}\right\} , \tag{2.7}$$

where, for example, u_{s1} denotes the displacement of node 1 in direction s. In addition, we introduce the vector

$$\underset{\sim}{\rho} = (u_{x1}, u_{y1}, \ldots , u_{x4}, u_{y4})^T \tag{2.8a}$$

containing the nodal displacements in directions x and y. Vectors $\underset{\sim}{\rho}_s$ and $\underset{\sim}{\rho}_n$ are expressed in terms of $\underset{\sim}{\rho}$ by the kinematic relations

$$\underset{\sim}{\rho}_s = \underset{\sim}{a}_s \, \underset{\sim}{C} \, \underset{\sim}{\rho} \quad , \tag{2.8b}$$

$$\underset{\sim}{\rho}_n = \underset{\sim}{a}_n \, \underset{\sim}{C} \, \underset{\sim}{\rho} \, , \tag{2.8c}$$

where

$$\underset{\sim}{C} = \text{diag}(\underset{\sim}{c}, \underset{\sim}{c}, \underset{\sim}{c}, \underset{\sim}{c}) \quad , \tag{2.8d}$$

and $\underset{\sim}{a}_s$ and $\underset{\sim}{a}_n$ are Boolean matrices, the elements of which are either 1 or 0; for example,

$$\underset{\sim}{a}_s = \begin{bmatrix} 1 & . & . & . & . & . & . \\ . & . & 1 & . & . & . & . \\ . & . & . & . & 1 & . & . \\ . & . & . & . & . & . & 1 \end{bmatrix} \quad . \tag{2.8e}$$

Next we define the constitutive model of the joint material. To this end we introduce the vectors

$$\underset{\sim}{\varepsilon} = (\varepsilon_s, \varepsilon_n)^T \quad , \tag{2.10a}$$

$$\underset{\sim}{f} = (f_s, f_n)^T \quad , \tag{2.10b}$$

where the elements of $\underset{\sim}{\varepsilon}$ are defined by (2.4), and f_s and f_n are shear and normal forces per unit length acting in directions s and n, respectively. Constitutive theories of discontinuities in rock defining the relation between $\underset{\sim}{f}$ and $\underset{\sim}{\varepsilon}$ were discussed by Goodman and Dubois [9]. In the present work the mechanical behavior of jointed rock is described by a nondilatant model in which shear and normal deformations are locally uncoupled. However, shear and normal modes of deformations are coupled indirectly through a Coulomb type failure criterion, as will be seen later. Goodman, Taylor and Brekke [7] proposed a constitutive model similar to the one introduced here.

In accordance with the experimental data reviewed in [9], the normal stress is related to the normal strain by an elastic, (i.e. path independent and nondissipative) law of the form

$$f_n = f_n(\varepsilon_n) \quad . \tag{2.11}$$

The particular function $f_n(\varepsilon_n)$ which is used in the present model is defined and illustrated in Figure 3. The tangent normal stiffness is defined by $k_n = df_n/d\varepsilon_n$. In Figure 3, d_o denotes the initial aperture of the joint, and f_{no} is the initial normal stress. The maximum tensile strength across the slip surfaces is assumed to be zero.

Shear deformations of the joint element are governed by friction. A one-dimensional elastic-plastic law was adopted for the constitutive model of the joint in shear modes of deformation, as indicated in Figure 4. Failure is specified according to the Mohr-Coulomb hypothesis

$$\left.\begin{aligned} f_{sy} &= C && \text{if } f_n \geq 0 \\ f_{sy} &= C - f_n \tan\phi && \text{if } f_n < 0 \end{aligned}\right\} , \tag{2.12}$$

where f_{sy} is the yield limit (peak shear strength), C is the cohesion, and ϕ the angle of friction. Shear failure occurs if $|f_s| \geq f_{sy}$. The residual strength during slip is given by αf_{sy}. α is called the stick-slip ratio; it controls the amount of energy dissipated during plastic shear motion (slip). The value of α is restricted by $0 < \alpha \leq 1$.

The state of stress at a point of the plane-strain continuum is defined by the stress vector

$$\underset{\sim}{\sigma} = (\sigma_{xx}, \sigma_{yy}, \sigma_{zz}, \sigma_{xy})^T \ , \tag{2.13}$$

where the z-axis is normal to the x,y-plane. The state of stress at a point on the fracture surface is defined by (2.10b), and $\underset{\sim}{f}$ is given in terms of $\underset{\sim}{\sigma}$ by the standard transformation

$$\underset{\sim}{f} = \underset{\sim}{D}\,\underset{\sim}{\sigma} \quad , \tag{2.14a}$$

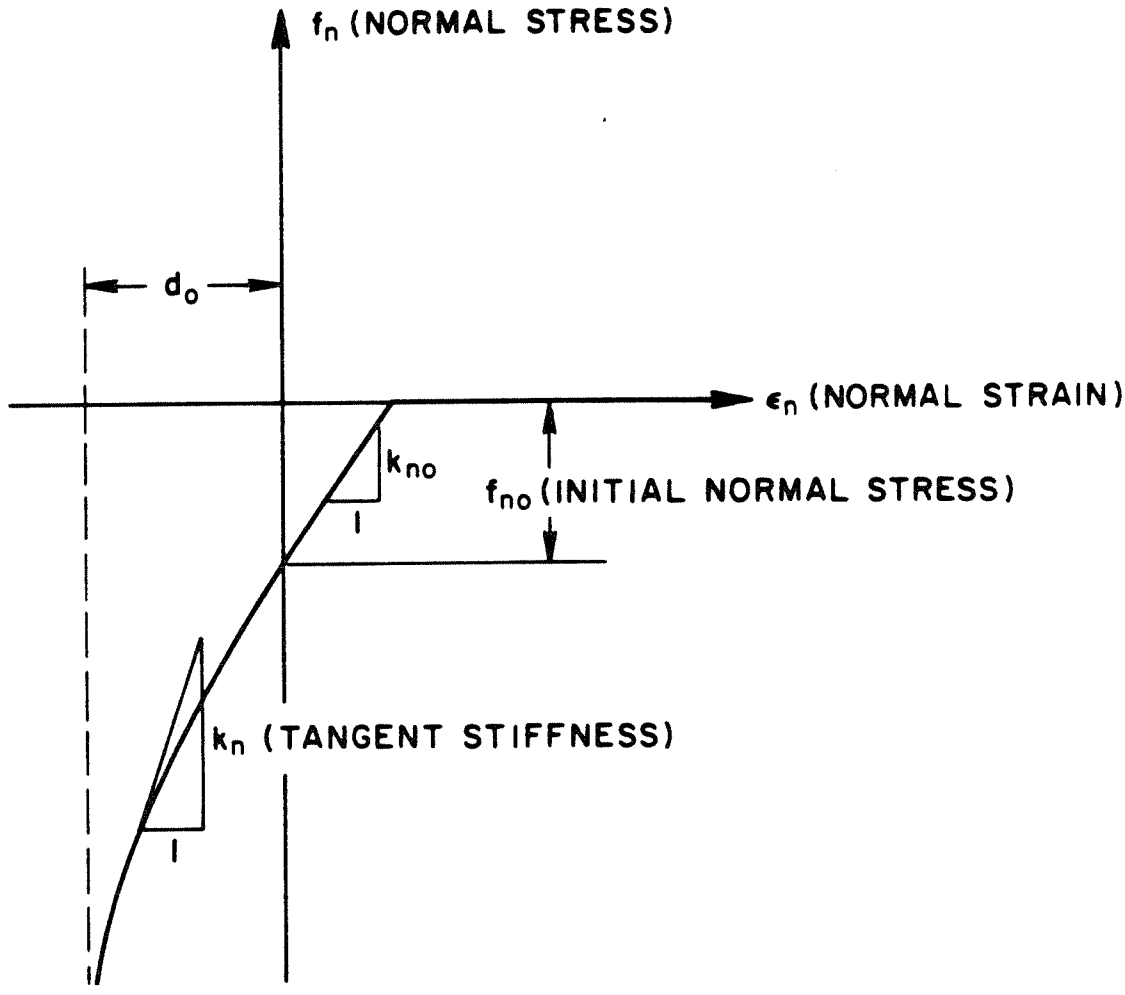

DEFINITION OF THE CONSTITUTIVE RELATION $f_n(\epsilon_n)$:

$$-d_o < \epsilon_n \leq 0: \qquad f_n = f_{no} + \frac{k_{no}\,\epsilon_n}{1 + \epsilon_n/d_o} \quad , \quad k_n = \frac{k_{no}}{(1 + \epsilon_n/d_o)^2}$$

$$0 \leq \epsilon_n \leq -\frac{f_{no}}{k_{no}}: \qquad f_n = f_{no} + k_{no}\,\epsilon_n \quad , \quad k_n = k_{no}$$

$$-\frac{f_{no}}{k_{no}} < \epsilon_n: \qquad f_n = 0 \quad , \quad k_n = 0$$

Fig. 3. Constitutive relation of joint element in contacting mode of deformation.

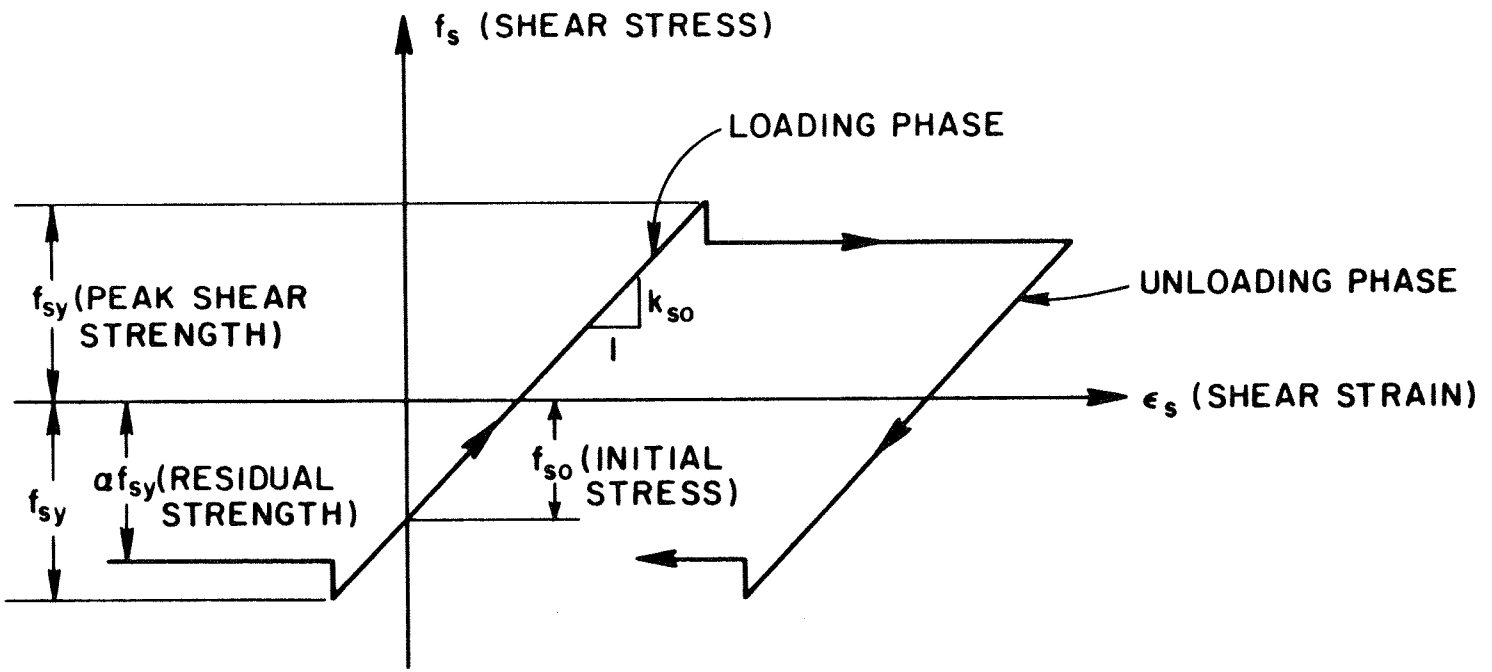

SHEAR FAILURE OCCURS IF $|f_s| \geq f_{sy}$, WHERE f_{sy} IS SPECIFIED BY THE MOHR-COULOMB HYPOTHESIS:

$f_{sy} = C$ IF $f_n \geq 0$

$f_{sy} = C + |f_n| \tan\phi$ IF $f_n < 0$

C = COHESION

ϕ = ANGLE OF FRICTION

Fig. 4. Constitutive relation of joint element in frictional mode of deformation.

where

$$\underset{\sim}{D} = \begin{bmatrix} -sc & sc & 0 & c^2 - s^2 \\ s^2 & c^2 & 0 & -2sc \end{bmatrix}, \tag{2.14b}$$

and $s = \sin\Theta$, $c = \cos\Theta$. Equations (2.14) are used to define the initial state of stress of a fracture surface such that it is statically compatible with the corresponding initial state of stress of the adjacent continuum.

Next we introduce the vector of nodal forces in global directions

$$\underset{\sim}{P} = (P_{x1}, P_{y1}, \ldots, P_{x4}, P_{y4})^T \quad , \tag{2.15}$$

and the vectors

$$\left.\begin{aligned} \underset{\sim}{P}_s &= (P_{s1}, P_{s2}, P_{s3}, P_{s4})^T \\ \underset{\sim}{P}_n &= (P_{n1}, P_{n2}, P_{n3}, P_{n4})^T \end{aligned}\right\} \quad , \tag{2.16}$$

where, for example, P_{s1} is the force at node 1 in direction s. The vector $\underset{\sim}{P}$ is related to $\underset{\sim}{P}_s$ and $\underset{\sim}{P}_n$ by the equilibrium equation

$$\underset{\sim}{P} = \underset{\sim}{C}^T (\underset{\sim}{a}_s^T \underset{\sim}{P}_s + \underset{\sim}{a}_n^T \underset{\sim}{P}_n), \tag{2.17}$$

and matrices $\underset{\sim}{C}$, $\underset{\sim}{a}_s$ and $\underset{\sim}{a}_n$ have been defined above; see expressions (2.8).

We want to establish the conditions of equilibrium between the nodal forces and the internal state of stress. By the principle of virtual displacements

$$\left.\begin{aligned} \underset{\sim}{P}_s &= \frac{L}{2} \int_{-1}^{1} \underset{\sim}{\phi}^T f_s \, d\xi \\ \underset{\sim}{P}_n &= \frac{L}{2} \int_{-1}^{1} \underset{\sim}{\phi}^T f_n \, d\xi \end{aligned}\right\} \quad . \tag{2.18}$$

Expressions (2.18) imply the following equations of statics:

$$\left.\begin{aligned} P_{n1} + P_{n4} &= 0 \\ P_{n2} + P_{n3} &= 0 \\ P_{n1} + P_{n2} + \frac{L}{2}\int_{-1}^{1} f_n \, d\xi &= 0 \end{aligned}\right\} . \tag{2.19}$$

Of course, the elements of $\underset{\sim}{P}_s$ are related by equations similar to (2.19).

The tangent stiffness matrix of the joint element is defined by

$$\underset{\sim}{k} = \frac{\partial \underset{\sim}{P}}{\partial \underset{\sim}{\rho}} . \tag{2.20}$$

Invoking the chain rule, by (2.8) and (2.17), (2.20) leads to

$$\underset{\sim}{k} = \underset{\sim}{C}^T (\underset{\sim s}{a}^T \underset{\sim s}{k}_s \underset{\sim s}{a}_s + \underset{\sim n}{a}^T \underset{\sim n}{k}_n \underset{\sim n}{a}_n) \underset{\sim}{C} , \tag{2.21a}$$

where

$$\left.\begin{aligned} \underset{\sim s}{k}_s &= \frac{\partial \underset{\sim s}{P}}{\partial \underset{\sim s}{\rho}} \\ \underset{\sim n}{k}_n &= \frac{\partial \underset{\sim n}{P}}{\partial \underset{\sim n}{\rho}} \end{aligned}\right\} . \tag{2.21b}$$

Since

$$\left.\begin{aligned} \frac{\partial f_s}{\partial \underset{\sim s}{\rho}} &= \frac{\partial f_s}{\partial \varepsilon_s}\frac{\partial \varepsilon_s}{\partial \underset{\sim s}{\rho}} = k_s \underset{\sim}{\phi} \\ \frac{\partial f_n}{\partial \underset{\sim n}{\rho}} &= \frac{\partial f_n}{\partial \varepsilon_n}\frac{\partial \varepsilon_n}{\partial \underset{\sim n}{\rho}} = k_n \underset{\sim}{\phi} \end{aligned}\right\} , \tag{2.22}$$

where k_s and k_n are the tangent moduli in shear and normal deformation, respectively, (2.21b) in conjunction with (2.18) yields

$$\left.\begin{aligned} \underset{\sim}{k}_s &= \frac{L}{2}\int_{-1}^{1} k_s\, \underset{\sim}{\phi}^T\, \underset{\sim}{\phi}\, d\xi \\ \underset{\sim}{k}_n &= \frac{L}{2}\int_{-1}^{1} k_n\, \underset{\sim}{\phi}^T\, \underset{\sim}{\phi}\, d\xi \end{aligned}\right\} \quad . \tag{2.23}$$

The mass density of material contained between slip surfaces is usually negligible compared to the density of the surrounding rock. Accordingly, we assume the joint element to have no mass.

The sum of the strain energy and the dissipated energy is defined by

$$U + E_D = \frac{L}{2}\int_{-1}^{1}\int_{\underset{\sim}{0}}^{\underset{\sim}{\varepsilon}} \underset{\sim}{f}^T\, d\underset{\sim}{\varepsilon}\, d\xi \quad . \tag{2.24}$$

Substituting (2.10) into (2.24), and making use of (2.5) and (2.18), we obtain

$$U + E_D = \int_{\underset{\sim}{0}}^{\underset{\sim}{\rho}_s} \underset{\sim}{P}_s^T\, d\underset{\sim}{\rho}_s + \int_{\underset{\sim}{0}}^{\underset{\sim}{\rho}_n} \underset{\sim}{P}_n^T\, d\underset{\sim}{\rho}_n \quad . \tag{2.25}$$

The shear behavior is governed by the elastic-plastic constitutive model defined in Figure 4. Correspondingly, we can decompose the shear strains into elastic and plastic components:

$$\varepsilon_s = \varepsilon_s^e + \varepsilon_s^p \quad . \tag{2.26}$$

In view of (2.4), (2.19) and (2.26) the strain energy

$$U = \int_0^{\varepsilon^e_{s1}} P_{s4}\, d\varepsilon^e_{s1} + \int_0^{\varepsilon^e_{s2}} P_{s3}\, d\varepsilon^e_{s2} + \int_0^{\varepsilon_{n1}} P_{n4}\, d\varepsilon_{n1} + \int_0^{\varepsilon_{n2}} P_{n3}\, d\varepsilon_{n2} \tag{2.27a}$$

and the dissipated energy

$$E_D = \int_0^{\varepsilon_{s1}^P} P_{s4}\, d\varepsilon_{s1}^P + \int_0^{\varepsilon_{s2}^P} P_{s3}\, d\varepsilon_{s2}^P \quad , \tag{2.27b}$$

where $\varepsilon_{s1} = \varepsilon_s\Big|_{\xi=-1}$, $\varepsilon_{s2} = \varepsilon_s\Big|_{\xi=1}$, etc. The numerical determination of U and E_D is based on expressions (2.27), as will be explained later.

Finally, we derive kinematically consistent nodal forces due to fluid pressure acting along the internal faces of the joint element. Invoking the small displacement assumption we establish the necessary equilibrium relations for the undeformed element. The internal pressure distribution is (approximately) given by

$$p = \psi_1(\xi)\, P_1 + \psi_2(\xi)\, p_2 \quad , \tag{2.28}$$

where p_1 and p_2 are the values of the pressure at sections 1,4 and 2,3, respectively. By the principle of virtual displacements, the nodal forces due to internal pressure are given by (2.17), with

$$\underset{\sim}{P}_s = \underset{\sim}{0} \tag{2.29a}$$

and

$$\underset{\sim}{P}_n = \frac{L}{2} \int_{-1}^{1} \underset{\sim}{\phi}^T p\, d\xi \ . \tag{2.29b}$$

2.2 COMPUTATIONAL CONSIDERATIONS

In this section we make some comments regarding the implementation of the joint element into a computer program. We begin with a remark concerning the programming of equations (2.17) and (2.21a). Matrices $\underset{\sim}{C}$, $\underset{\sim}{a}_s$ and $\underset{\sim}{a}_n$ are introduced for notational convenience only. Matrix multiplications are not performed in the procedures assembling matrices $\underset{\sim}{P}$ and $\underset{\sim}{k}$.

Next we discuss methods for computing the vectors of internal forces (2.18) and the stiffness matrices (2.23). The integrals in equations (2.18) and (2.23) are most conveniently evaluated numerically. A two-point integration rule was found to be adequate in terms of accuracy and computational efficiency. A one-point integration rule does not suffice, since it amounts to an averaging procedure which neglects all but the constant terms in the integrands of (2.18) and (2.23). Among the commonly known two-point quadrature methods, the Gaussian integration rule provides the highest accuracy when continuous functions are integrated. However, it introduces coupling between the degrees of freedom of adjacent nodal points along the fracture surfaces, (e.g. between the degrees of freedom of nodes 1 and 2 in Figure 2). This, in turn, can prevent the iterative solution algorithm from converging into dynamic states of equilibrium. For example, we tested the two-point Gaussian formulation in a series of problems which were supposed to simulate nonlinear displacement oscillations of a planar fault system in shear (i.e. frictional modes of deformation). The equilibrium iterations consistently failed to converge whenever one or more mass points passed the point of maximum amplitude and started to accelerate in reversed direction; see example 4 in Chapter 5. However, we have been able to simulate nonlinear frictional motions in a physically meaningful way by performing the state determination at the nodal points of the joint element. This was accomplished by choosing a two-point integration rule which samples at the two sections $\xi = \pm 1$. This integration rule is defined by the following example: consider the function $g(\xi)$, then

$$\int_{-1}^{1} g(\xi)\, d\xi \approx g(-1) + g(1) \quad . \tag{2.30}$$

Obviously, this quadrature method is integrating smooth functions less accurately than the Gaussian formula. However, it provides the correct coupling between interacting points across fracture surfaces, such that the phenomena of contacting and stick-slip friction are simulated by our discrete model in a physically meaningful way.

Explicit forms of (2.18) and (2.23) corresponding to the nodal-point integration rule are

$$\left.\begin{aligned} \underset{\sim}{P}_s &= \frac{L}{2}\,(-f_{s1},\ -f_{s2},\ f_{s2},\ f_{s1})^T \\ \underset{\sim}{P}_n &= \frac{L}{2}\,(-f_{n1},\ -f_{n2},\ f_{n2},\ f_{n1})^T \end{aligned}\right\} \tag{2.31}$$

and

$$\underset{\sim}{k}_s = \frac{L}{2}\begin{bmatrix} k_{s1} & 0 & 0 & -k_{s1} \\ & k_{s2} & -k_{s2} & 0 \\ & & k_{s2} & 0 \\ \text{(symmetric)} & & & k_{s1} \end{bmatrix}, \tag{2.32a}$$

$$\underset{\sim}{k}_n = \frac{L}{2}\begin{bmatrix} k_{n1} & 0 & 0 & -k_{n1} \\ & k_{n2} & -k_{n2} & 0 \\ & & k_{n2} & 0 \\ \text{(symmetric)} & & & k_{n1} \end{bmatrix}, \tag{2.32b}$$

respectively, where $f_{s1} = f_s\big|_{\xi=-1}$, $f_{s2} = f_s\big|_{\xi=1}$, $k_{s1} = k_s(\varepsilon_{s1})$, $k_{s2} = k_s(\varepsilon_{s2})$, etc. With this we conclude the discussion of equations (2.18) and (2.23).

The energies stored and dissipated in the joint element are determined by equations (2.27). The integrals in (2.27) are evaluated incrementally. For this purpose each integral in (2.27) is written in an incremental form which can be defined as follows:

$$\int_0^{\varepsilon} P(\varepsilon)\, d\varepsilon = \sum_{i=0,1,2,\ldots} \int_{\varepsilon_i}^{\varepsilon_{i+1}} P(\varepsilon)\, d\varepsilon \quad . \tag{2.33a}$$

The integrals extending over the individual increments are evaluated approximately using the trapezoidal rule:

$$\int_{\varepsilon_i}^{\varepsilon_{i+1}} P(\varepsilon)\, d\varepsilon \approx [P(\varepsilon_i) + P(\varepsilon_{i+1})](\varepsilon_{i+1} - \varepsilon_i)/2 \quad . \tag{2.33b}$$

Finally, it should be mentioned that the vector of nodal forces due to internal pressure, defined by (2.17) in conjunction with (2.29), is explicitly given by

$$\underset{\sim}{P} = \underset{\sim}{b}\,\underset{\sim}{p} \quad , \tag{2.34}$$

where

$$\underset{\sim}{p} = (p_1, p_2)^T \quad , \tag{2.35}$$

and $\underset{\sim}{b} = \underset{\sim}{N}\,\underset{\sim}{e}$. Matrix $\underset{\sim}{N}$ is defined by

$$\underset{\sim}{N} = \begin{bmatrix} -\underset{\sim}{n} & \underset{\sim}{0} \\ \underset{\sim}{0} & -\underset{\sim}{n} \\ \underset{\sim}{0} & \underset{\sim}{n} \\ \underset{\sim}{n} & \underset{\sim}{0} \end{bmatrix} \quad , \tag{2.36a}$$

where

$$\underset{\sim}{n} = (-\sin\Theta, \cos\Theta)^T \tag{2.36b}$$

is the unit vector in direction n (see Figure 2). Furthermore, matrix

$$\underset{\sim}{e} = [e_{ij}] = [\frac{L}{2} \int_{-1}^{1} \psi_i \, \psi_j \, d\xi] = \frac{L}{6} \begin{bmatrix} 2 & 1 \\ 1 & 2 \end{bmatrix}, \tag{2.37}$$

in which i,j = 1,2, and the interpolation functions ψ_i are defined by (2.2).

2.3 THE GOVERNING INITIAL VALUE PROBLEM

The dynamic behavior of the fractured rock mass is described by the following system of second order differential equations of motion:

$$\underset{\sim}{M} \, \ddot{\underset{\sim}{u}} + \underset{\sim}{K}(\underset{\sim}{u}) = \underset{\sim}{R} + \underset{\sim}{B} \, \underset{\sim}{H} \quad . \tag{2.38}$$

In (2.38) $\underset{\sim}{u}$ and $\ddot{\underset{\sim}{u}}$ denote, respectively, the vectors of nodal displacements and accelerations, $\underset{\sim}{M}$ is the mass matrix of the idealized solid material, and

$$\underset{\sim}{K}(\underset{\sim}{u}) = \underset{\sim}{K}_S \, \underset{\sim}{u} + \underset{\sim}{K}_J(\underset{\sim}{u}) \quad . \tag{2.39}$$

In (2.39) $\underset{\sim}{K}_S$ is the (constant) stiffness matrix of the solid material and $\underset{\sim}{K}_J(\underset{\sim}{u})$ is the vector of nodal forces representing the internal reactions of the deformed fractures. As was mentioned in the introduction, four-node isoparametric quadrilateral elements are used to discretize the continuous domains. The corresponding mass, stiffness and load matrices are defined in the relevant literature; see for example [12]. Since the joint elements have been assumed massless, $\underset{\sim}{M}$ represents the mass of the continuous rock only.

The vector-valued forcing function $\underset{\sim}{R} = \underset{\sim}{R}(t)$ is due to all prescribed loads acting on the system, such as body and surface forces, or time dependent displacement boundary conditions. The fluid pressure inside the fracture walls is accounted for by the term $\underset{\sim}{B} \, \underset{\sim}{H}$ in (2.38), where $\underset{\sim}{H}$ is the vector of nodal heads defined in Chapter 3.

The assemblage procedure establishing matrices $\underset{\sim}{M}$, $\underset{\sim}{K}$, $\underset{\sim}{B}$, etc. in terms of the corresponding element matrices is standard; see for example [12]. The initial value problem of (2.38) consists of finding the vector valued function $\underset{\sim}{u}(t)$ satisfying (2.38) at all times $t \in [0, t_{max}]$, $t_{max} > 0$ and

$$\left.\begin{aligned} \underset{\sim}{u}(0) &= \underset{\sim}{d} \\ \dot{\underset{\sim}{u}}(0) &= \underset{\sim}{v} \end{aligned}\right\} , \tag{2.40}$$

where $\underset{\sim}{d}$ and $\underset{\sim}{v}$ are given initial data. It is to be noted that the discrete model described by (2.38) dissipates energy through frictional deformations of the fracture surfaces only. Dissipation due to viscous properties of the material has been ignored.

Equation (2.38) constitutes one equation for the unknowns $\underset{\sim}{u}$ and $\underset{\sim}{H}$. To make the problem well posed a second equation is needed. It will be derived in the following chapter.

3. FLUID-FLOW NETWORK ANALYSIS

The system of fractures formed by idealized slip surfaces through non-porous rock masses constitutes the network of flow paths. The rationality of a fluid-flow model similar to the one presented here was discussed by Gale et al. [8]. A typical part of a mesh of flow elements is schematically depicted in Figure 1. The topology and geometry of the network of fluid-flow elements are defined by the mesh of joint elements, such that to each joint element corresponds a fluid element with the same topological and geometrical data. Both the geometry and the coordinate system of a typical fluid-flow element are defined in Figure 5. Of course, the plane of symmetry of the element is in general parallel to direction s; see Figure 2. For notational convenience, without loss of generality, the theory of the flow element will be presented for the special case s = x.

3.1 DERIVATION OF THE FLOW ELEMENT

In Figure 5 q denotes the flow rate (i.e.,transported liquid volume per unit time), and h is the average head at a cross-section x. At any station x along the flow path, the cross-sectional area available for fluid flow is given by

$$S = A \bullet d \quad , \tag{3.1a}$$

where

$$d = d_o + \varepsilon_n \ . \tag{3.1b}$$

In (3.1) d = d(x,t) is the width of the flow channel, A its average depth measured in direction z (i.e. normal to the x,y plane), and ε_n is the normal strain of the joint element defined by (2.4). Hence, the function S(x,t) is uniquely defined by $\underset{\sim}{u}(t)$ and the kinematic assumptions (2.1) and

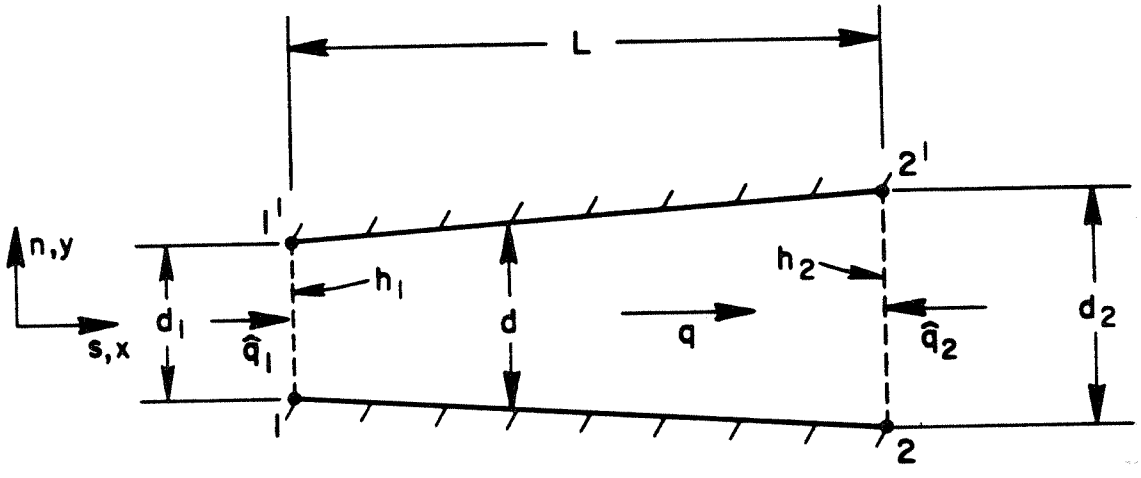

q = FLOW RATE (AVERAGED OVER THE CROSS-SECTION)
h = HEAD (AVERAGED OVER THE CROSS-SECTION)
d = WIDTH OF FLOW CHANNEL

Fig. 5. Geometry and coordinate system of a fluid flow element.

(2.2). This implies that within each element S(x,t) is linear in x. The assumptions A = const. and d << L allow us to ignore the nonaxial velocity components v_y and v_z. Furthermore, we assume the velocity profile to be parabolic, that is $v_x(y)$ is quadratic in y and $v_x(-y) = v_x(y)$, where v_x is the velocity of a fluid particle in direction x. By these assumptions we implicitly violate the boundary conditions $v_x = \dot{u}_s$ and $v_y = \dot{u}_n$ at the lateral faces of the flow channel. This is justified since we are employing a quasi one-dimensional formulation in which only averaged quantities occur. For example, the mean velocity v, defined by

$$v = \frac{1}{S} \int_S v_x(y)\, dS \quad , \tag{3.2a}$$

is related to the flow rate by

$$v = q/S \quad . \tag{3.2b}$$

The principle of conservation of mass can be expressed in the form

$$\frac{\partial q}{\partial x} + \frac{\partial S}{\partial t} = 0 \quad . \tag{3.3}$$

Moreover, assuming sufficiently small velocities, the inertia forces and the convective terms in the Navier-Stokes equation can be neglected such that the combined momentum and constitutive differential equation of incompressible viscous flow becomes

$$k \frac{\partial h}{\partial x} + q = 0 \quad . \tag{3.4}$$

In (3.4) $k = \gamma\, Sd^2/12\mu$ is the area permeability for a parabolic flow profile, h is the head, γ is the specific weight and μ the viscosity of the fluid.

Neglecting gravity effects, the pressure is given by $p = \gamma h - \rho v^2/2$, where ρ is the fluid density. However, since we neglected the effect of

convective and inertia terms in the Navier-Stokes equation, for consistency, we also drop the kinetic energy term in the expression for p and simply use

$$p = \gamma h \quad . \tag{3.5}$$

Combining (3.3) and (3.4) yields the partial differential equation

$$\frac{\partial}{\partial x} \left(k \frac{\partial h}{\partial x}\right) = \frac{\partial S}{\partial t} \tag{3.6}$$

which determines the state of the fluid at any section x; see Figure 5. The boundary value problem consists of finding the function h(x,t) which satisfies (3.6) and one boundary condition at each end of the flow element depicted in Figure 5. Admissible boundary conditions are

$$\left.\begin{aligned} h = \hat{h}_1 \text{ or } q = \hat{q}_1 \quad &\text{at section 1} \\ h = \hat{h}_2 \text{ or } q = -\hat{q}_2 \quad &\text{at section 2} \end{aligned}\right\} \quad . \tag{3.7}$$

The sign convention used in (3.7) is defined in Figure 5, and prescribed quantities are characterized by a superposed hat.

In order to derive the finite element equations of the above boundary value problem, it has to be rewritten in weak form. Denoting the boundary points by "b", the points where q is specified by b_q and the prescribed boundary flow rates by $\hat{q}$, the weak (or Galerkin) form of (3.6) is given by

$$-\int_0^L \left[\frac{\partial}{\partial x} \left(k \frac{\partial h}{\partial x}\right) - \frac{\partial S}{\partial t}\right] \psi(x)\, dx + \oint_{b_q} (\hat{q}-q)\, \Psi(x)\, db = 0 \ , \tag{3.8}$$

which must hold for all admissible functions $\psi(x)$; see Strang and Fix [13]. The first step towards the discretization of (3.8) is to admit only a finite number of test functions $\psi_i(x)$. Here i = 1, 2 and the functions ψ_i are

defined by (2.2) in terms of ξ. Replacing $\psi(x)$ by $\psi_i(\xi)$, changing variables and integrating by parts, equation (3.8) becomes

$$\frac{2}{L}\int_{-1}^{1}\frac{\partial\psi_i}{\partial\xi}\,k\,\frac{\partial h}{\partial\xi}\,d\xi+\frac{L}{2}\int_{-1}^{1}\psi_i\,\frac{\partial S}{\partial t}\,d\xi+\oint_{b_q}\hat{q}\,\psi_i\,db+\oint_{b_h}q\,\psi_i\,db=0 \qquad (3.9)$$

for i = 1,2. For notational simplicity we use the same symbols for the continuous and the approximating discrete forms. It is important to note that in (3.8) and (3.9) the function $h(\xi,t)$ is assumed to satisfy the boundary conditions at b_h. Expanding h in terms of the test functions yields

$$h(\xi,t)=\psi_j(\xi)\;\;h_j(t)\quad,\qquad\text{(sum)} \qquad (3.10)$$

where summation over j is implied and h_j is the (average) head at section j, j = 1,2. Substitution of (3.10) into (3.9) leads to

$$\frac{2}{L}\int_{-1}^{1}k\,\frac{\partial\psi_i}{\partial\xi}\,\frac{\partial\psi_j}{\partial\xi}\,d\xi\,h_j+\frac{L}{2}\int_{-1}^{1}\psi_i\,\frac{\partial S}{\partial t}\,d\xi+\oint_{b_q}\psi_i\,\hat{q}\,db+\oint_{b_h}\psi_i\,q\,db=0 \qquad (3.11)$$

for i = 1,2. If the cross-sectional area is expressed in terms of its values at nodes 1 and 2 as

$$S(\xi,t)=\psi_j(\xi)\;S_j(t)\quad,\qquad\text{(sum)} \qquad (3.12)$$

(3.11) can be integrated exactly and the result may be written in the matrix form

$$\underset{\sim}{k}_F\,\underset{\sim}{h}+\underset{\sim}{e}\,\dot{\underset{\sim}{S}}=\underset{\sim}{q}\quad. \qquad (3.13)$$

In (3.13) $\underset{\sim}{e}$ is defined by (2.37), and

$$\underset{\sim}{k}_F = \frac{\bar{k}}{L} \begin{bmatrix} 1 & -1 \\ -1 & 1 \end{bmatrix} \quad , \tag{3.14a}$$

$$\underset{\sim}{h} = (h_1, h_2)^T \quad , \tag{3.14b}$$

$$\underset{\sim}{q} = (q_1, q_2)^T \quad , \tag{3.14c}$$

$$\underset{\sim}{S} = (S_1, S_2)^T \quad . \tag{3.14d}$$

In (3.14a)

$$\bar{k} = \gamma A \bar{d}^3/(12\mu) \quad , \tag{3.14e}$$

where

$$\bar{d}^3 = (d_1^3 + d_1^2 d_2 + d_1 d_2^2 + d_2^3)/4 \quad . \tag{3.14f}$$

Note that the "hats" on the nodal quantities in (3.14b,c) are omitted for notational convenience.

A basic question with regard to the finite element fluid-flow equations is the following: Do equations (3.13) determine states of fluid flow which approximately (i.e. in a discrete fashion) satisfy the governing differential equation (3.6)? To answer this question we compare the sum and the difference of equations (3.13) with the associated differential equations (3.3) and (3.4), respectively. The sum yields

$$\frac{q_2 - q_1}{L} + \frac{\dot{S}_1 + \dot{S}_2}{2} = 0 \quad , \tag{3.15a}$$

and the difference can be written in the form

$$\bar{k} \quad \frac{h_2 - h_1}{L} + \frac{q_1 + q_2}{2} = L(\dot{S}_1 - \dot{S}_2)/12 \quad . \tag{3.15b}$$

Obviously, (3.15a) is a first order difference approximation to (3.3); (3.15b) is a first order difference formula for (3.4), provided that $L|\dot{S}_2 - \dot{S}_1|$ is sufficiently small compared to the left hand terms in (3.15b). Thus, the form (3.13) is consistent with (3.6) and the discrete solution converges to

the exact one as $L \to 0$. However, we are concerned about the accuracy of the discrete solution for positive values of L, for which the term $L(\dot{S}_2 - \dot{S}_1)$ may be large enough to have significant effects on the approximating finite element system. In order to eliminate this potential source of error, matrix $\underset{\sim}{e}$ in (3.13) is replaced by

$$\underset{\sim}{e}_F = \frac{L}{4}\begin{bmatrix} 1 & 1 \\ 1 & 1 \end{bmatrix} \quad . \tag{3.16}$$

$\underset{\sim}{e}_F$ is an averaging operator which guarantees that the right hand term in (3.15b) is equal to zero for all L. The vector $\dot{\underset{\sim}{S}}$ in (3.13) can be expressed in terms of the nodal velocities $\dot{\underset{\sim}{\rho}}$ of the joint element:

$$\dot{\underset{\sim}{S}} = A\, \underset{\sim}{N}^T\, \dot{\underset{\sim}{\rho}} \quad , \tag{3.17}$$

$\underset{\sim}{N}$ being defined by (2.36). Using (3.16) and (3.17) in (3.13) we get

$$\underset{\sim}{k}_F\, \underset{\sim}{h} + \underset{\sim}{b}_F^T\, \dot{\underset{\sim}{\rho}} = \underset{\sim}{q} \quad , \tag{3.18}$$

where $\underset{\sim}{\rho}$ is defined by (2.8), and $\underset{\sim}{b}_F = A\, \underset{\sim}{N}\, \underset{\sim}{e}_F$. The matrix $\underset{\sim}{b}_F$ is explicitly given by

$$\underset{\sim}{b}_F^T = \frac{A}{4}\begin{bmatrix} \Delta y & -\Delta x & \Delta y & -\Delta x & -\Delta y & \Delta x & -\Delta y & \Delta x \\ \Delta y & -\Delta x & \Delta y & -\Delta x & -\Delta y & \Delta x & -\Delta y & \Delta x \end{bmatrix} \quad . \tag{3.19}$$

3.2 STATEMENT OF THE GOVERNING EQUATIONS

In order to determine the pressure and flow rate distribution in the entire flow network, matrix equations such as (3.18) for all fluid-flow elements have to be assembled and the resulting system of differential equations has to be solved. Assembly conditions are defined and illustrated in Figure 6, in which three flow elements are attached to a nodal point I. The first condition enforces compatibility, that is all individual heads at adjacent element nodes must be equal. The second condition insures

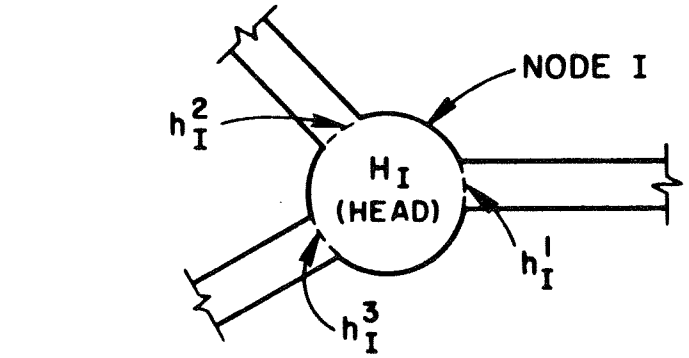

BALANCE OF MOMENTA AT NODE I:

$h_I^e = H_I \ (e = 1,2,3)$

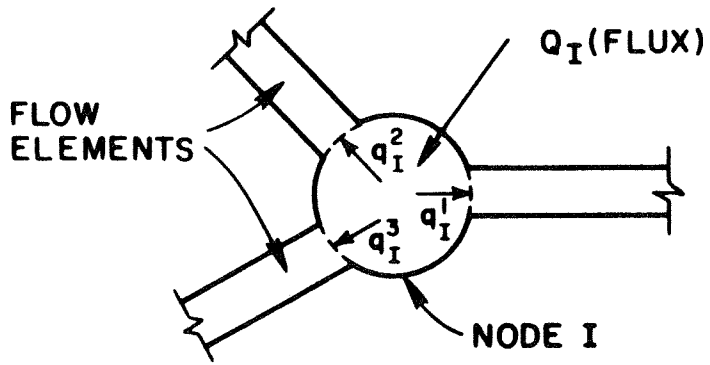

BALANCE OF MASS AT NODE I:

$\sum_{e=1}^{3} q_I^e = Q_I$

FLOW BOUNDARY CONDITIONS REQUIRE EITHER H_I OR Q_I TO BE PRESCRIBED.

Fig. 6. Assembly conditions for fluid flow elements.

conservation of mass. Expressing $\underset{\sim}{\rho}$ in terms of $\underset{\sim}{u}$ and assembling all flow elements, we end up with the system of first order differential equations

$$\underset{\sim}{B}_F^T \dot{\underset{\sim}{u}} + \underset{\sim}{K}_F \underset{\sim}{H} = \underset{\sim}{Q} \quad . \tag{3.20}$$

In (3.20) $\underset{\sim}{H}$ is the vector of nodal heads, and $\dot{\underset{\sim}{u}}$ denotes the vector of nodal velocities. The vector valued function $\underset{\sim}{Q}(t)$ represents prescribed external flux of fluid entering the system, as well as the effects of time dependent pressure boundary conditions. The term $\underset{\sim}{B}_F^T \dot{\underset{\sim}{u}}$ in (3.20) accounts for the effects of wall motions normal to the direction of fluid flow. The flow conductivity matrix $\underset{\sim}{K}_F$ depends nonlinearly on the fracture deformations: $\underset{\sim}{K}_F(\underset{\sim}{u})$. The assembly procedure which sets up the matrices $\underset{\sim}{B}_F$, $\underset{\sim}{K}_F$, etc. in terms of the corresponding element matrices defined above is standard. In fact, it can be shown that the fluid-flow network analysis is analogous to a displacement analysis of a plane truss. In this analogy the head and the flow rate in the fluid flow element correspond to the axial displacement and the force in the truss bar element, respectively.

4. SOLUTION ALGORITHMS FOR THE NONLINEAR DYNAMIC STRESS-FLOW ANALYSIS

The behavior of the entire solid-fluid system of fractured rock is described by equations (2.38) and (3.20). The interactive effects between the solid and fluid domains in the model are represented by the term $\underset{\sim}{B}\,\underset{\sim}{H}$ in (2.38), and by the terms $\underset{\sim}{B}_F^T\,\dot{\underset{\sim}{u}}$ and $\underset{\sim}{K}_F\,\underset{\sim}{H}$ in (3.20). To determine the state of the system at all times $t \in (0, t_{max}]$ we have to find the response histories $\underset{\sim}{u}(t)$ and $\underset{\sim}{H}(t)$ which simultaneously satisfy equations (2.38) and (3.20). Due to the inherent complexity and nonlinearity of this sytem of coupled differential equations we cannot hope to find a closed form solution, but instead must resort to numerical techniques which generate approximate solutions in a step-by-step fashion.

4.1. TIME DISCRETIZATION

The Newmark family of step-by-step integration formulas [11] was found to be a versatile and efficient tool for integrating equations (2.38) and (3.20). Application of the Newmark methods amounts to replacing these differential equations by the following algebraic equations of recursive form:

$$\left.\begin{aligned} \underset{\sim}{d}_{n+1} &= \underset{\sim}{d}_n + \Delta t\, \underset{\sim}{v}_n + \Delta t^2[(1/2 - \beta)\, \underset{\sim}{a}_n + \beta\, \underset{\sim}{a}_{n+1}] \\ \underset{\sim}{v}_{n+1} &= \underset{\sim}{v}_n + \Delta t[(1 - \gamma)\, \underset{\sim}{a}_n + \gamma\, \underset{\sim}{a}_{n+1}] \end{aligned}\right\}, \qquad (4.1a)$$

$$\underset{\sim}{M}\,\underset{\sim}{a}_{n+1} + \underset{\sim}{K}(\underset{\sim}{d}_{n+1}) = \underset{\sim}{R}_{n+1} + \underset{\sim}{B}\,\underset{\sim}{H}_{n+1}, \qquad (4.1b)$$

$$\underset{\sim}{B}_F^T\,\underset{\sim}{v}_{n+1} + \underset{\sim}{K}_F(\underset{\sim}{d}_{n+1})\,\underset{\sim}{H}_{n+1} = \underset{\sim}{Q}_{n+1}, \qquad (4.1c)$$

$$\left.\begin{aligned} \underset{\sim}{d}_o &= \underset{\sim}{d} \\ \underset{\sim}{v}_o &= \underset{\sim}{v} \end{aligned}\right\}, \qquad (4.1d)$$

$$\left.\begin{aligned} \underset{\sim}{H}_o &= \underset{\sim}{K}_F^{-1}(\underset{\sim}{d}_o)\,[\underset{\sim}{Q}_o - \underset{\sim}{B}_F^T\,\underset{\sim}{v}_o] \\ \underset{\sim}{a}_o &= \underset{\sim}{M}^{-1}\,[\underset{\sim}{R}_o + \underset{\sim}{B}\,\underset{\sim}{H}_o - \underset{\sim}{K}(\underset{\sim}{d}_o)] \end{aligned}\right\}, \qquad (4.1e)$$

where $n = 0, 1, 2, \ldots, N - 1$. N is the number of time steps, $\Delta t = t_{max}/N$, $\underset{\sim}{d}_n$, $\underset{\sim}{v}_n$, $\underset{\sim}{a}_n$ and $\underset{\sim}{H}_n$ are the approximations to $\underset{\sim}{u}(t_n)$, $\dot{\underset{\sim}{u}}(t_n)$, $\ddot{\underset{\sim}{u}}(t_n)$ and $\underset{\sim}{H}(t_n)$, respectively. Furthermore, $t_n = n\,\Delta t$, $\underset{\sim}{R}_n = \underset{\sim}{R}(t_n)$, $\underset{\sim}{Q}_n = \underset{\sim}{Q}(t_n)$, and β, γ are free parameters which govern the stability and numerical dissipation of the Newmark algorithms. The choice $\beta = 1/4$ and $\gamma = 1/2$ corresponds to the constant average acceleration method, which is also known as the trapezoidal rule or the Crank-Nicolson method. This algorithm is the most accurate unconditionally stable member of the Newmark family, and does not possess numerical dissipation. Further elaborations on these points and more technical details about step-by-step integration formulas in general, as well as the Newmark methods in particular, can be found in [11, 14].

Substitution of (4.1a) into (4.1b) and (4.1c) yields

$$\alpha_o \underset{\sim}{M}\, \underset{\sim}{d}_{n+1} + \underset{\sim}{K}(\underset{\sim}{d}_{n+1}) = \tilde{\underset{\sim}{R}}_{n+1} + \underset{\sim}{B}\, \underset{\sim}{H}_{n+1} \quad , \tag{4.2a}$$

$$\alpha_1 \underset{\sim}{B}_F^T\, \underset{\sim}{d}_{n+1} + \underset{\sim}{K}_F(\underset{\sim}{d}_{n+1})\, \underset{\sim}{H}_{n+1} = \tilde{\underset{\sim}{Q}}_{n+1} \quad , \tag{4.2b}$$

where

$$\tilde{\underset{\sim}{R}}_{n+1} = \underset{\sim}{R}_{n+1} + \underset{\sim}{M}\,(\alpha_o\, \underset{\sim}{d}_n + \alpha_2\, \underset{\sim}{v}_n + \alpha_3\, \underset{\sim}{a}_n) \quad , \tag{4.2c}$$

$$\tilde{\underset{\sim}{Q}}_{n+1} = \underset{\sim}{Q}_{n+1} + \underset{\sim}{B}_F^T\,(\alpha_1\, \underset{\sim}{d}_n + \alpha_4\, \underset{\sim}{v}_n + \alpha_5\, \underset{\sim}{a}_n), \tag{4.2d}$$

$$\underset{\sim}{a}_{n+1} = \alpha_o\,(\underset{\sim}{d}_{n+1} - \underset{\sim}{d}_n) - \alpha_2\, \underset{\sim}{v}_n - \alpha_3\, \underset{\sim}{a}_n \quad , \tag{4.2e}$$

$$\underset{\sim}{v}_{n+1} = \alpha_1\,(\underset{\sim}{d}_{n+1} - \underset{\sim}{d}_n) - \alpha_4\, \underset{\sim}{v}_n - \alpha_5\, \underset{\sim}{a}_n \quad , \tag{4.2f}$$

and

$$\left.\begin{aligned} &\alpha_o = 1/(\Delta t^2 \beta); \quad \alpha_1 = \gamma/(\Delta t\, \beta); \quad \alpha_2 = 1/(\Delta t\, \beta) \quad ; \\ &\alpha_3 = 1/(2\beta) - 1; \; \alpha_4 = \gamma/\beta - 1 \; ; \quad \alpha_5 = \Delta t\,(\gamma/2\beta - 1) \end{aligned}\right\} \quad . \tag{4.3}$$

Expressions (4.2) represent a system of nonlinear algebraic equations of recursive form. Computational techniques for solving such systems will be discussed after the following remarks concerning the computation of the total energy stored in the continuous domains of the mesh.

4.2 ENERGY OF THE SOLID MATERIAL

The kinetic and strain energies of the discrete model at time t_n are

$$E_K^n = 1/2\ \underset{\sim}{v}_n^T\ \underset{\sim}{M}\ \underset{\sim}{v}_n \tag{4.4a}$$

and

$$U_s^n = 1/2\ \underset{\sim}{d}_n^T\ \underset{\sim}{K}_s\ \underset{\sim}{d}_n + \underset{\sim}{F}_s^T(\underset{\sim}{\sigma}_o)\ \underset{\sim}{d}_n \quad , \tag{4.4b}$$

respectively, where $\underset{\sim}{M}$ is the mass matrix of the solid material and $\underset{\sim}{K}_s$ is defined by (2.39). Both $\underset{\sim}{M}$ and $\underset{\sim}{K}_s$ are assembled from the mass and stiffness matrices of the isoparametric quadrilateral elements. The vector $\underset{\sim}{F}_s(\underset{\sim}{\sigma}_o)$ in (4.4b) represents the nodal forces due to the initial state of stress of the continuous rock. In (2.38) the effect of initial stresses is implicitly accounted for through $\underset{\sim}{R}$. In the computer program matrix operations (4.4) are most efficiently performed at the element level.

4.3 SOLUTION STRATEGY FOR THE ANALYSIS OF COUPLED SOLID-FLUID SYSTEMS

In order to generate the entire response history the system of nonlinear algebraic equations (4.2) has to be solved at the set of discrete points t_{n+1}, $n = 0,1,2, \ldots, N-1$. Thus, at any instant of time t_n, it is essentially the same problem that has to be solved as in the case of the steady-state analysis.

The fixed-point iteration technique which was used by Gale et al. [8] to simulate quasi-static processes was found to be suitable for the dynamic analysis also. This technique amounts to solving equations (4.2b) for $\underset{\sim}{H}_{n+1}$ with $\underset{\sim}{d}_{n+1}$ fixed, and then holding $\underset{\sim}{H}_{n+1}$ fixed during the iterative solution of (4.2a) for $\underset{\sim}{d}_{n+1}$. This cycle is repeated until convergence is reached. Convergence implies that the fluid pressure distribution is (numerically) compatible with the state of stress throughout the deformable rock.

We define the fixed point iteration technique by rewriting (4.2) in the form

$$\alpha_o \underset{\sim}{M}\, \underset{\sim}{d}_{n+1}^{j+1} + \underset{\sim}{K}(\underset{\sim}{d}_{n+1}^{j+1}) = \underset{\sim}{\tilde{R}}_{n+1} + \underset{\sim}{B}\, \underset{\sim}{H}_{n+1}^{j} \quad , \tag{4.5a}$$

$$\underset{\sim}{K}_F(\underset{\sim}{d}_{n+1}^{j})\, \underset{\sim}{H}_{n+1}^{j} = \underset{\sim}{\tilde{Q}}_{n+1} - \alpha_1\, \underset{\sim}{B}_F^T\, \underset{\sim}{d}_{n+1}^{j} \quad , \tag{4.5b}$$

where $j = 0, 1, 2, \ldots$. To start the iteration we set $j = 0$ and $\underset{\sim}{d}_{n+1}^{o} = \underset{\sim}{d}_n$. Each cycle consists of two steps: first equation (4.5b) is solved for $\underset{\sim}{H}_{n+1}^{j}$, and then $\underset{\sim}{d}_{n+1}^{j+1}$ is determined from (4.5a). The fixed point iteration is terminated if $||\underset{\sim}{H}_{n+1}^{j+1} - \underset{\sim}{H}_{n+1}^{j}|| < \varepsilon_F\, ||\underset{\sim}{H}_{n+1}^{j}||$, where ε_F is a given convergence tolerance and $||\ldots||$ denotes a vector norm. The norm presently used in the computer program is called max-norm; it is defined by $||\underset{\sim}{H}||_{max} = \max\{|H_k|,\ k = 1, 2, 3, \ldots\}$, where H_k is the kth element of vector $\underset{\sim}{H}$. In most applications convergence was achieved in one or two iteration cycles, depending on the required accuracy. The converged vectors $\underset{\sim}{H}_{n+1}^{j+1}$ and $\underset{\sim}{d}_{n+1}^{j+1}$ are denoted by $\underset{\sim}{H}_{n+1}$ and $\underset{\sim}{d}_{n+1}$, respectively.

The second step in each fixed point iteration cycle consists of solving the nonlinear algebraic equations (4.5a) for $\underset{\sim}{d}_{n+1}^{j+1}$ in terms of $\underset{\sim}{H}_{n+1}^{j}$. In [8] a secant stiffness iteration method was adopted for the corresponding step in the analysis of steady-state configurations. For the simulation of nonlinear dynamic processes of the presently considered type the secant method was not found to work satisfactorily. Instead, the Newton-Raphson algorithm proved to be a reliable and efficient iterative technique to determine dynamic equilibrium configurations of the fractured rock system. A modification of the Newton-Raphson method, the so called constant stiffness or load perturbation method is discussed in [9] with regard to applications of similar type as considered here. In the remainder of this chapter we define and discuss the Newton-Raphson method within the context of equations (4.5a).

For notational simplicity we rewrite (4.5a) in the form

$$\tilde{\underset{\sim}{F}}(\underset{\sim}{d}) - \underset{\sim}{R}^* = \underset{\sim}{0} \quad , \tag{4.6a}$$

in which $\underset{\sim}{d} = \underset{\sim n+1}{d^{j+1}}$,

$$\underset{\sim}{R}^* = \tilde{\underset{\sim n+1}{R}} + \underset{\sim}{B}\, \underset{\sim n+1}{H^j} \tag{4.6b}$$

and

$$\tilde{\underset{\sim}{F}}(\underset{\sim}{d}) = (\alpha_o \underset{\sim}{M} + \underset{\sim s}{K})\, \underset{\sim}{d} + \underset{\sim J}{K}(\underset{\sim}{d}) \quad , \tag{4.6c}$$

where $\underset{\sim s}{K}$ and $\underset{\sim J}{K}$ are defined by (2.39). To solve (4.6a) for $\underset{\sim}{d}$ we use the Newton-Raphson method; it is defined by the following recursive formulas:

$$\left.\begin{aligned} \underset{\sim}{DK}^i\, \underset{\sim}{\Delta d}^{i+1} &= \underset{\sim}{R}^* - \tilde{\underset{\sim}{F}}(\underset{\sim}{d}^i) \\ \underset{\sim}{d}^{i+1} &= \underset{\sim}{d}^i + \underset{\sim}{\Delta d}^{i+1} \end{aligned}\right\} \quad , \; i = 0,1,2,\ldots . \tag{4.7}$$

The starting values are given by $\underset{\sim}{d}^o = \underset{\sim n+1}{d^j}$, and the tangent stiffness matrix

$$\underset{\sim}{DK}^i = \alpha_o \underset{\sim}{M} + \underset{\sim s}{K} + \underset{\sim J}{DK}^i \quad , \tag{4.8a}$$

where

$$\underset{\sim J}{DK}^i = \left.\frac{\partial \underset{\sim J}{K}}{\partial \underset{\sim}{d}}\right|_{\underset{\sim}{d}=\underset{\sim}{d}^i} \quad . \tag{4.8b}$$

$\underset{\sim J}{DK}^i$ is assembled from the corresponding joint element stiffness matrices defined by (2.21). Equilibrium is achieved, and the iteration is terminated, if

$$||\underset{\sim}{R}^* - \tilde{\underset{\sim}{F}}(\underset{\sim}{d}^{i+1})||_2 < \varepsilon_s \quad , \tag{4.9a}$$

where $||\ldots||_2$ is the L_2 vector norm defined by $||\underset{\sim}{F}||_2 = (\sum_k F_k^2)^{1/2}$, $\underset{\sim}{F} = (F_1, F_2, \ldots)^T$, and ε_s is a given convergence tolerance. Instead of (4.9a) the following convergence criteria may be used:

$$||\underset{\sim}{\Delta d}^{i+1}||_2 < \varepsilon_s\, ||\underset{\sim}{d}^i||_2 \quad . \tag{4.9b}$$

The advantage of (4.9a) compared to (4.9b) is that it directly monitors the absolute magnitude of the out-of-balance forces. However, since ε_s must be adjusted to the order of magnitude of the numbers occurring in the force vectors this criterion is inconvenient. This drawback is overcome by using (4.9b). Once the Newton-Raphson iterations converged, we set $\underset{\sim}{d}_{n+1}^{j+1} \equiv \underset{\sim}{d}^{i+1}$, where $\underset{\sim}{d}^{i+1}$ is the converged solution of (4.6). The modified Newton-Raphson method is derived from (4.7) by simply using the same tangent stiffness matrix over a number of iteration cycles. Hence, for the modified version, replace (4.7) by

$$\left.\begin{aligned} \underset{\sim}{DK}^{o}\ \Delta\underset{\sim}{d}^{i+1} &= \underset{\sim}{R}^{*} - \underset{\sim}{\tilde{F}}(\underset{\sim}{d}^{i}) \\ \underset{\sim}{d}^{i+1} &= \underset{\sim}{d}^{i} + \Delta\underset{\sim}{d}^{i+1} \end{aligned}\right\} \quad , \ i = 0,1,2,\ldots. \qquad (4.10)$$

A flow chart of the complete solution procedure described in this chapter is shown in Figure 7. Finally, we note that the quasi-static, steady-state solution is obtained if in (4.3) $\alpha_k = 0$, $k = 0,1,2,3,4,5$.

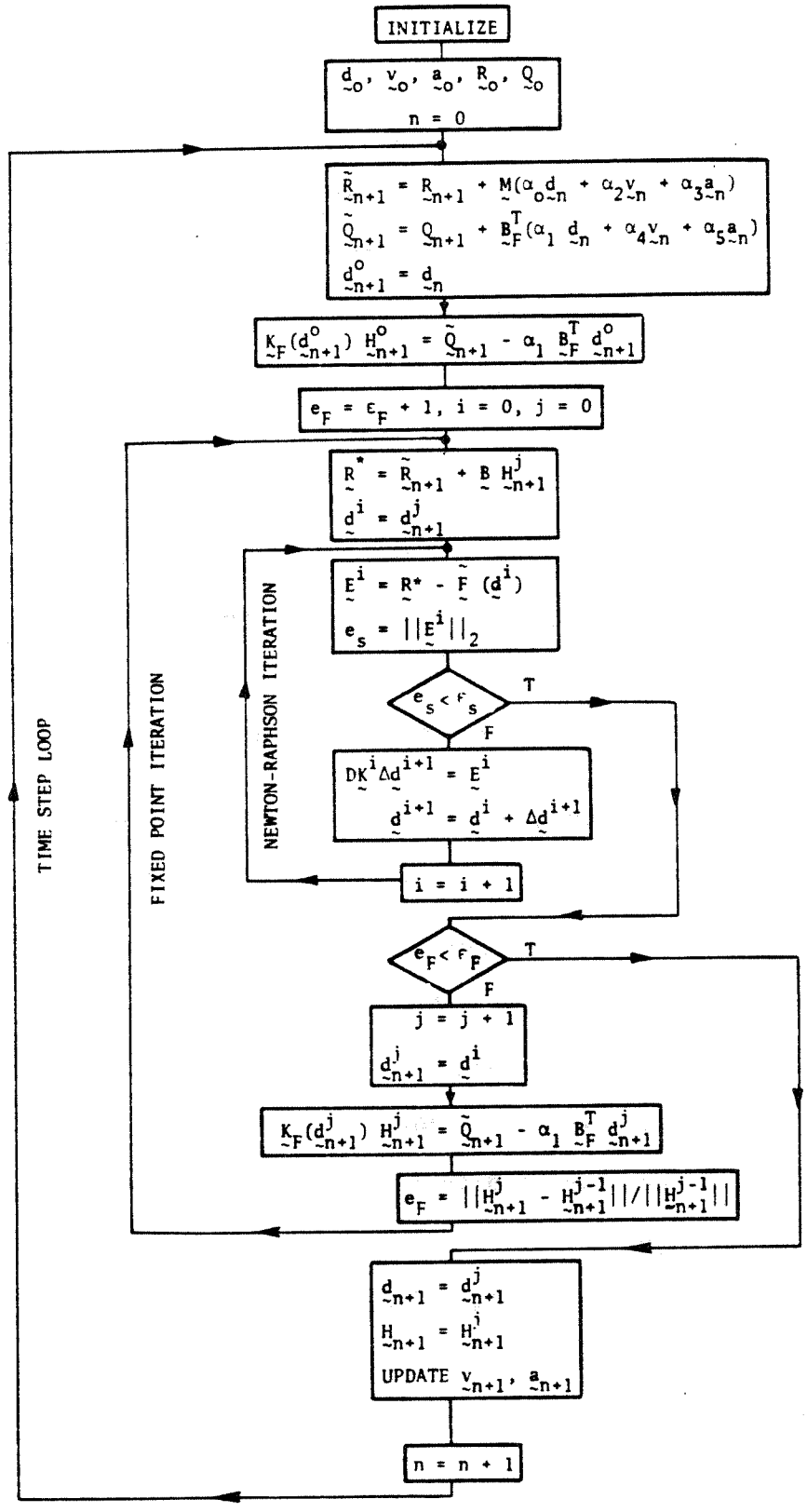

Fig. 7. Flow chart of the complete solution procedure for coupled stress-flow analysis.

5. APPLICATIONS

A number of simplified problems have been solved to test the computer program and to demonstrate the method of analysis described in Chapters 2 to 4. Problems 1 and 2 are designed to test the release and locking mechanism in pure shear modes of deformation under quasi-static and dynamic conditions. Problems 3 to 5 demonstrate the feasibility of using the present model to study the effects of injection and removal of fluid along prestressed fracture surfaces, and serve as an introduction to similar problems of more complex nature. Although the computer program features lumped and consistent mass matrices, the examples discussed subsequently in this chapter are all based on lumped mass approximations. For the solution of the dynamic problems the trapezoidal rule (i.e. $\beta = 1/4$, $\gamma = 1/2$ in (4.3)) has been used.

5.1 AN ELASTICALLY SUPPORTED RIGID BLOCK SLIDING BETWEEN TWO JOINTS

Consider the problem of Figure 8: An elastically supported rigid block is sliding between two joints in a quasi-static motion caused by a prescribed forcing function P(t). This problem is intended to test the release and locking mechanisms of the joint elements in pure shear deformations, and to illustrate and compare secant and tangent stiffness methods of solution. The finite element mesh as well as the function P(t) are defined in Figure 8.

The modulus of elasticity and Poisson ratio of the elastic elements are, respectively, $E = 0.05$ and $\nu = 0$. The constitutive relations of the joint element are defined in Figures 3 and 4, where $f_n = f_{no} = 0$, $f_{so} = 0$, $k_{no} = 1$, $k_{so} = 1$, $d_o = 1$, $\phi = 45°$, $C = 0.1$, $\alpha = 0.8$. Since $f_n = 0$, the peak shear strength f_{sy} equals C. The stiffness of this single degree-of-freedom system depends on the linearly elastic lateral elements and on the nonlinear friction laws built into the joint elements.

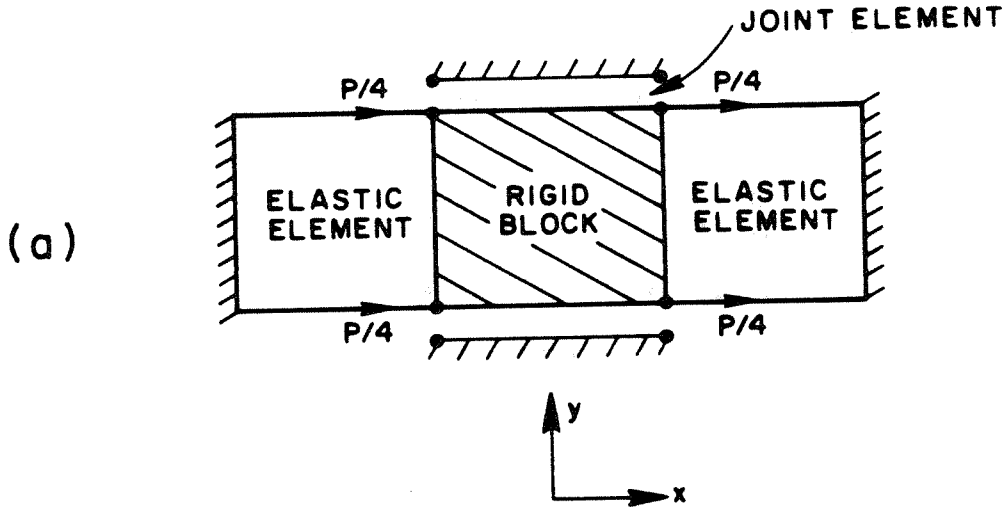

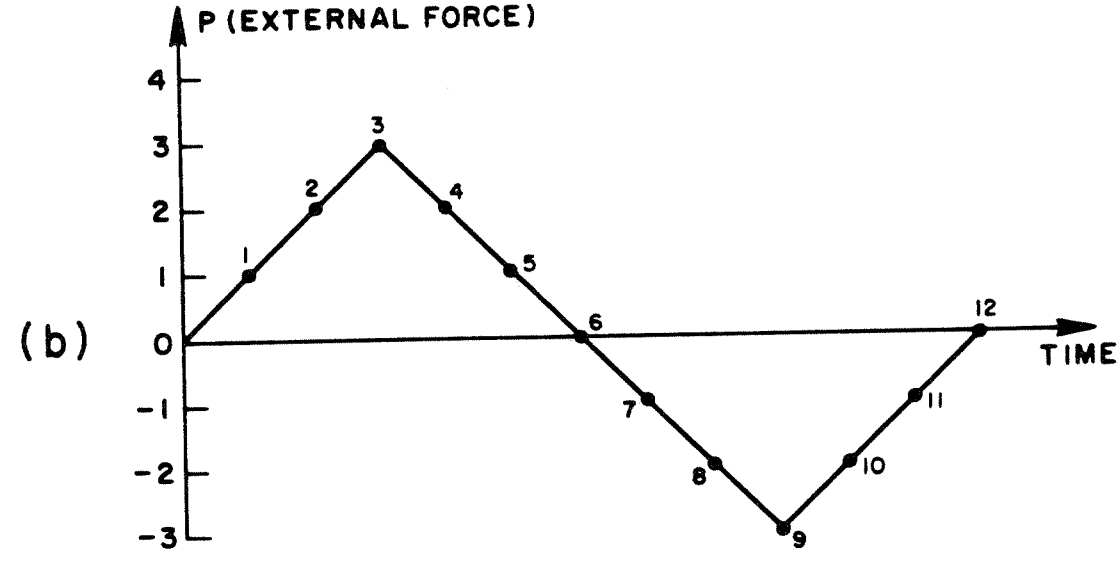

Fig. 8. Elastically supported rigid block sliding between joints in a quasi-static forced motion. (a) Problem set-up. (b) Forcing function.

The solution history in the displacement-force configuration space is depicted in Figure 9. At any instant of time the internal resisting force $F(u_x)$ is seen to be in equilibrium with the external force $P(t)$. The results of Figure 9 are obtained by the Newton-Raphson iteration technique as described in Chapter 4. This technique was found to be very efficient in solving nonlinear algebraic equations of the type considered here. It automatically takes advantage of locally linear behavior. In addition, only one extra iteration is needed to advance the solution over a nonlinear event. For example, in Figure 9 only one iteration is needed to advance from state 4 to state 5, and it took two iterations to advance from point 6 to point 7.

The basic differences between a secant stiffness iteration technique, the constant stiffness method and the Newton method are schematically indicated in Figure 10. For the sake of clearness, in Figure 10, $\alpha = 1$ and the initially stress-free system is loaded by $P = P_3$; see Figure 8. Both the secant and constant tangent stiffness methods would need a very large number of iterations to come close to the exact solution, whereas the Newton method finds it in just two iterations.

As indicated in Figure 9, the entire response history $F(u_x)$ includes several loading and unloading phases. The secant stiffness method, as defined in [8,9], was not found to be applicable to nonlinear problems which include unloading of the type encountered here. The Newton method easily handles the unloading case in two iterations, provided that an overshooting control is preventing the computed solutions to diverge too far away from the correct equilibrium configuration.

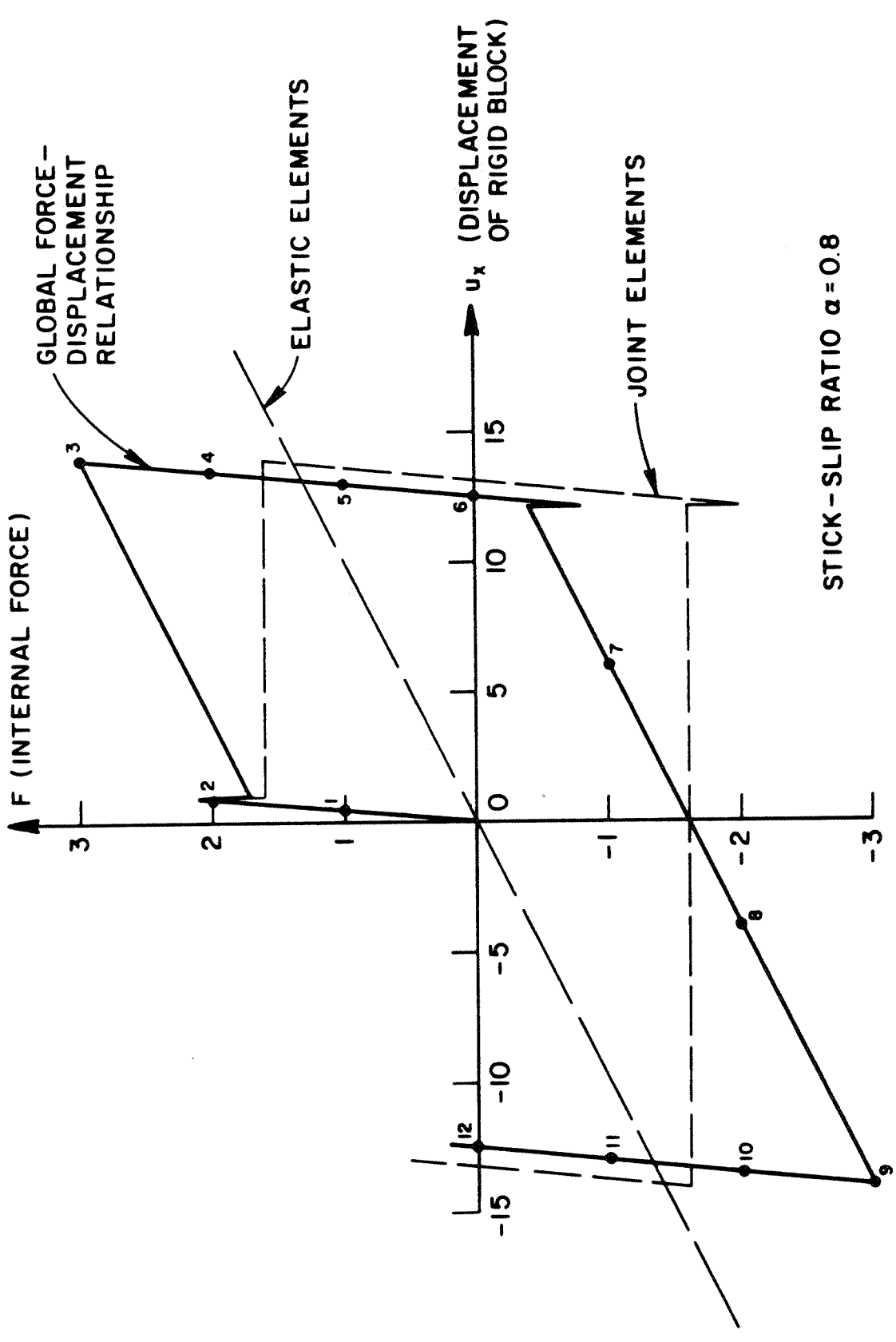

Fig. 9. Equilibrium configurations of rigid block in quasi-static forced motion.

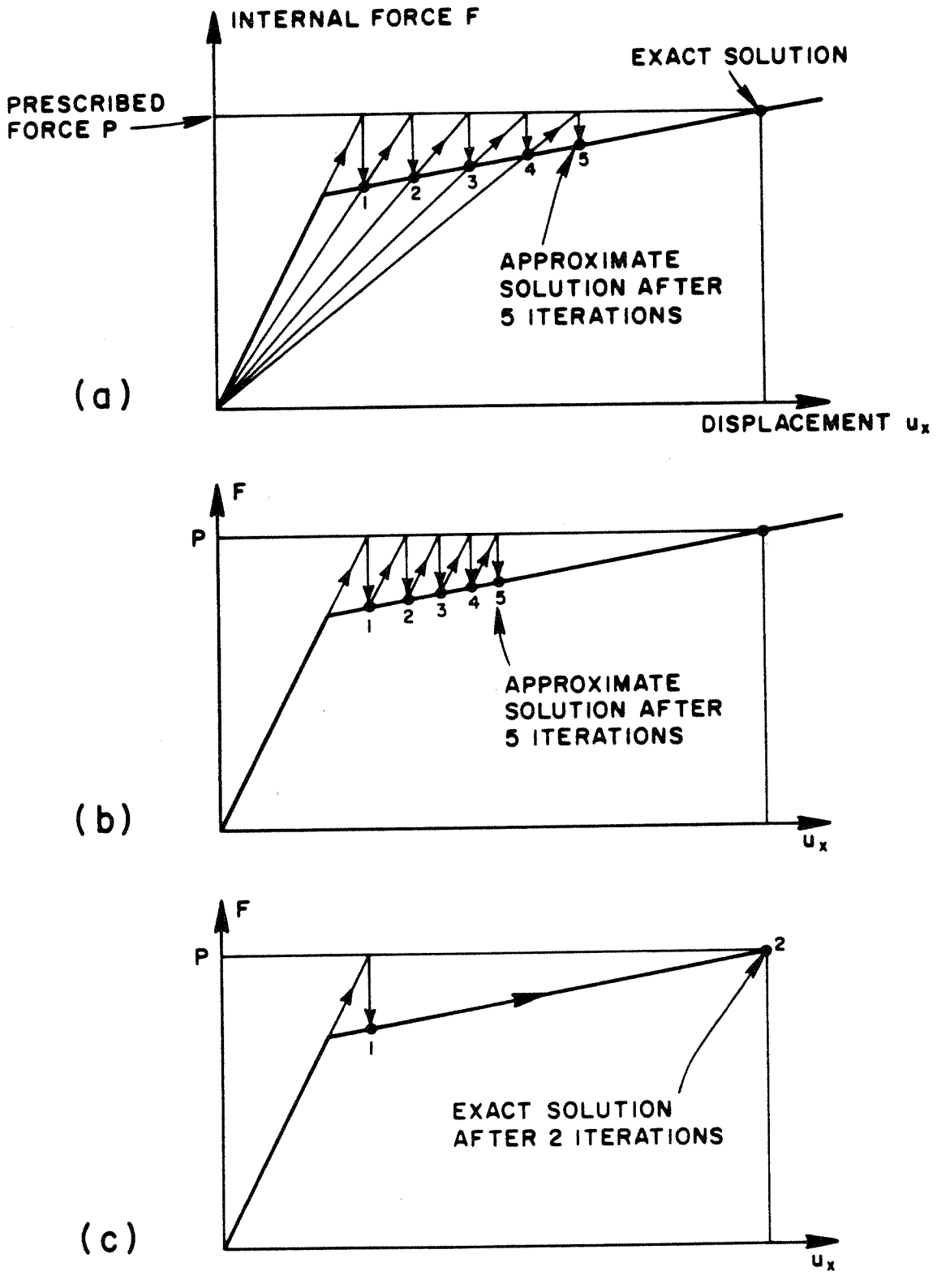

Fig. 10. Solutions to a bilinear static problem by (a) the secant stiffness method, (b) the constant stiffness or modified Newton method, and (c) the tangent stiffness or Newton method.

5.2 SINGLE DEGREE-OF-FREEDOM OSCILLATORY SYSTEM

A single degree-of-freedom oscillatory system is used to test the release and locking mechanisms of the joint elements as well as the solution algorithms, under nonlinear dynamic conditions. The problem set-up is shown in Figure 11: A rigid block is sliding between two joints in a dynamic motion which consists of a forced and a free phase. The finite element mesh and the forcing function P(t) are defined in Figure 11.

The constitutive relations of the joint elements are defined in Figures 3 and 4 with the following data: $f_n = f_{no} = -1$, $f_{so} = 0$, $k_{no} = 1$, $k_{so} = 1/2$, $d_o = 1$, $\phi = 45°$, $C = 0$, $\alpha = 1$. The mass of the rigid block is assumed to be one and the time step size $\Delta t = 1/10$. Since $C = 0$ and $f_n = -1$, the peak shear strength f_{sy} equals one. As in the previous example, no fluid effects are considered. If the density of the fluid is set to zero, the computer program automatically skips the determination of the fluid flow and the fixed-point iteration is switched off.

The displacement of the rigid block as a function of time is shown in Figure 12. For the purpose of comparison, the displacement reponse history according to a linear joint constitutive law is included in the same figure. As indicated in Figure 11, the motion is forced during the first 3.4 seconds, and it is free thereafter. The amplitudes of the free oscillator can be read off Figure 12. They are $u_{max} = 4.3$ for linear elastic friction and $u_{max} - u_{steady\ state} = 2$ for the elastic-plastic friction mechanisms. The difference between the linear and the nonlinear oscillations is due to the energy dissipated during plastic sliding. The slip-phases are indicated in Figure 12, and the force-displacement history is plotted in Figure 13. Figures 12 and 13 indicate that the rigid mass slides into a new permanently displaced equilibrium position, $u_{steady\ state}$, about which it oscillates

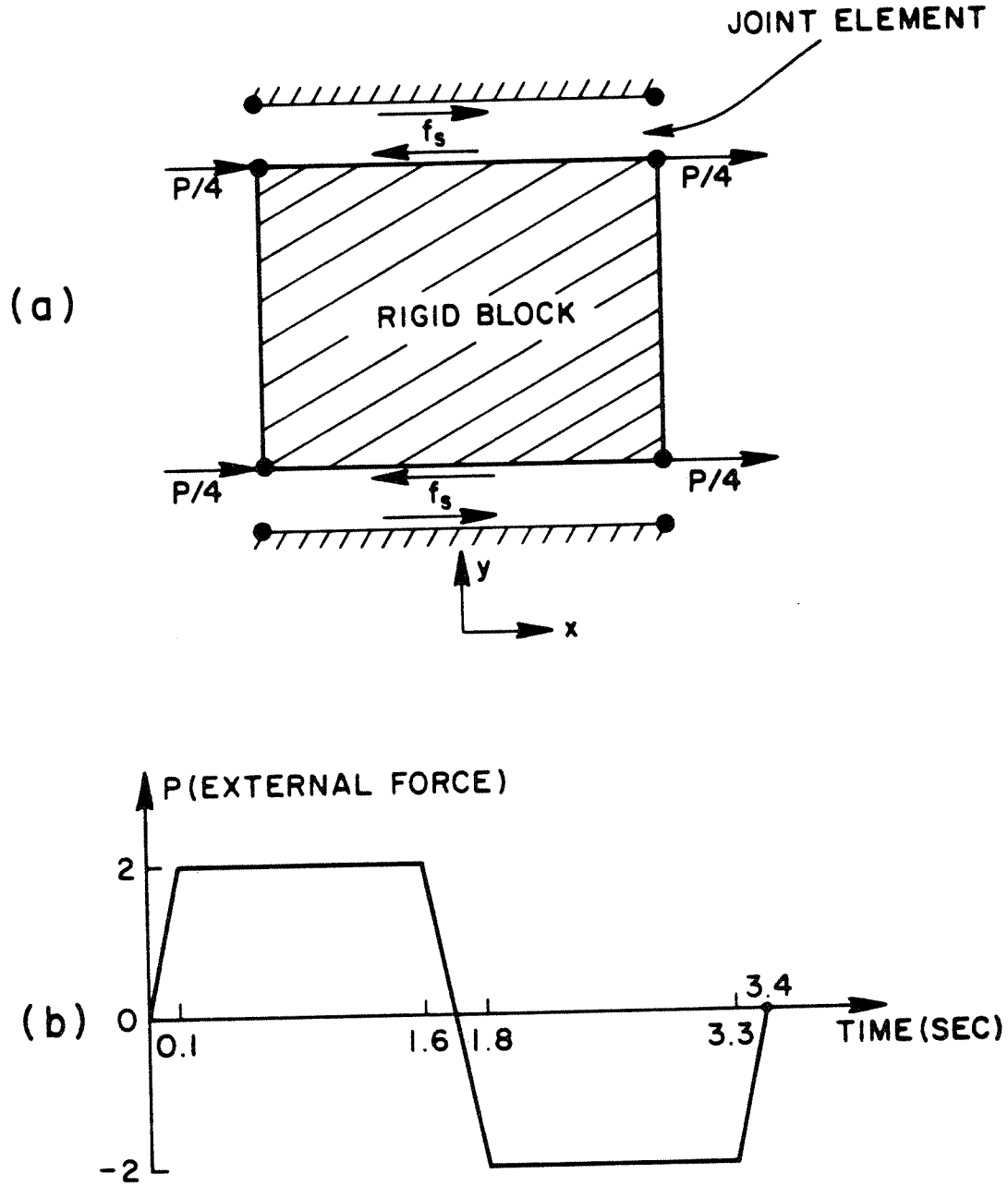

Fig. 11. Rigid block sliding between joints in forced and free dynamic motions. (a) Problem set-up. (b) Forcing function.

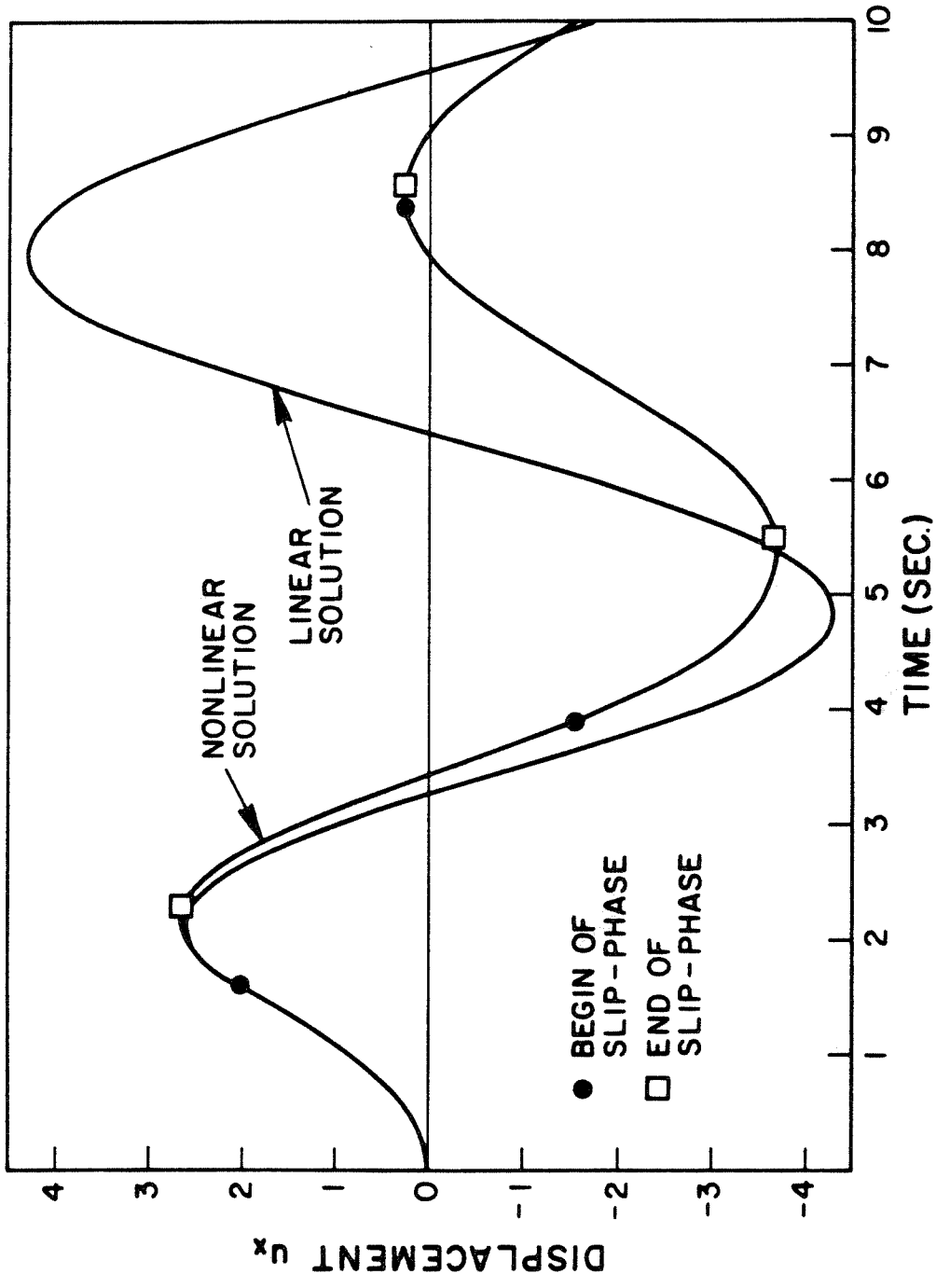

Fig. 12. Displacement response histories of rigid block oscillator.

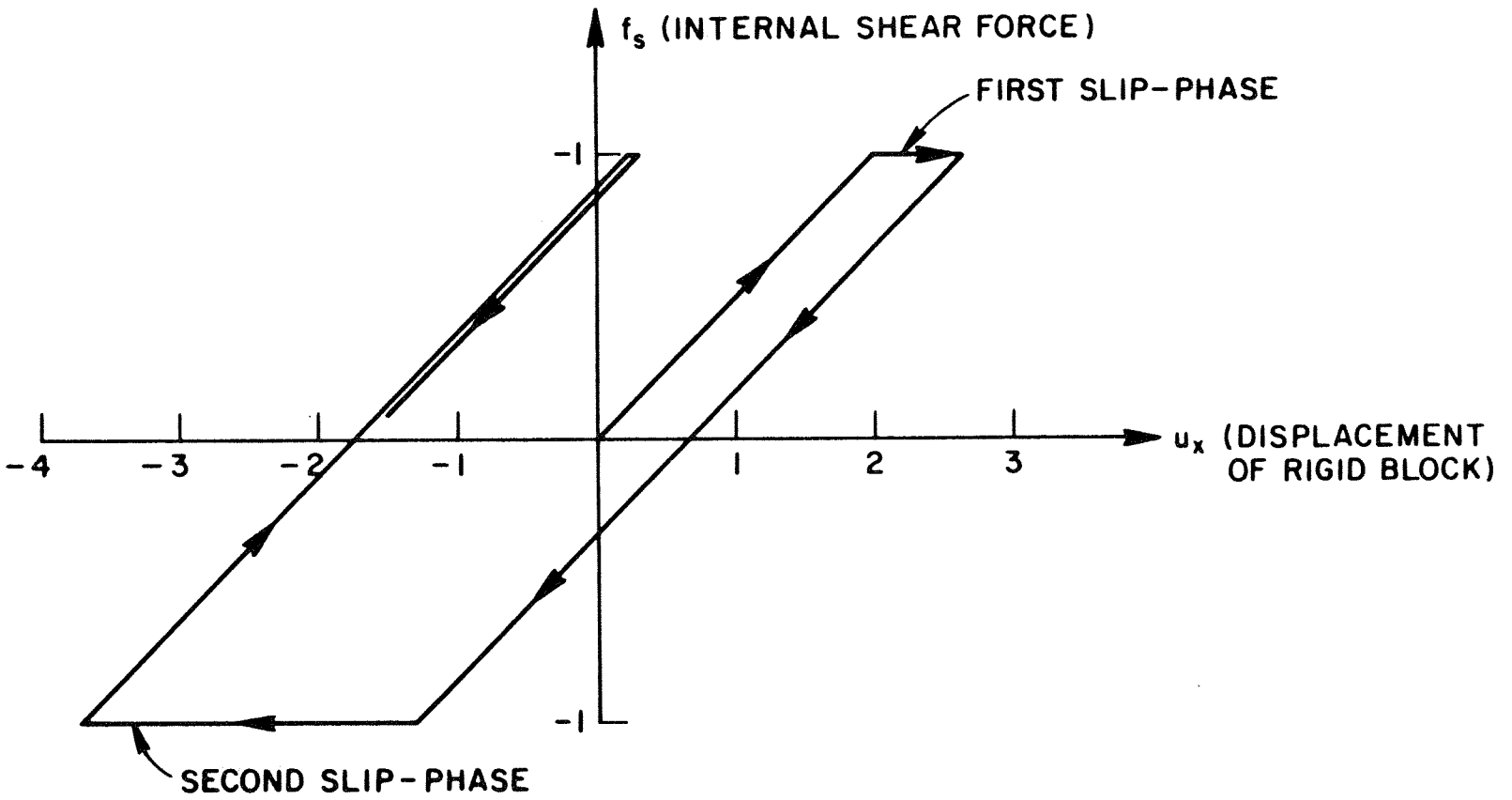

Fig. 13. Internal shear force in joint elements as a function of the displacement of the rigid block.

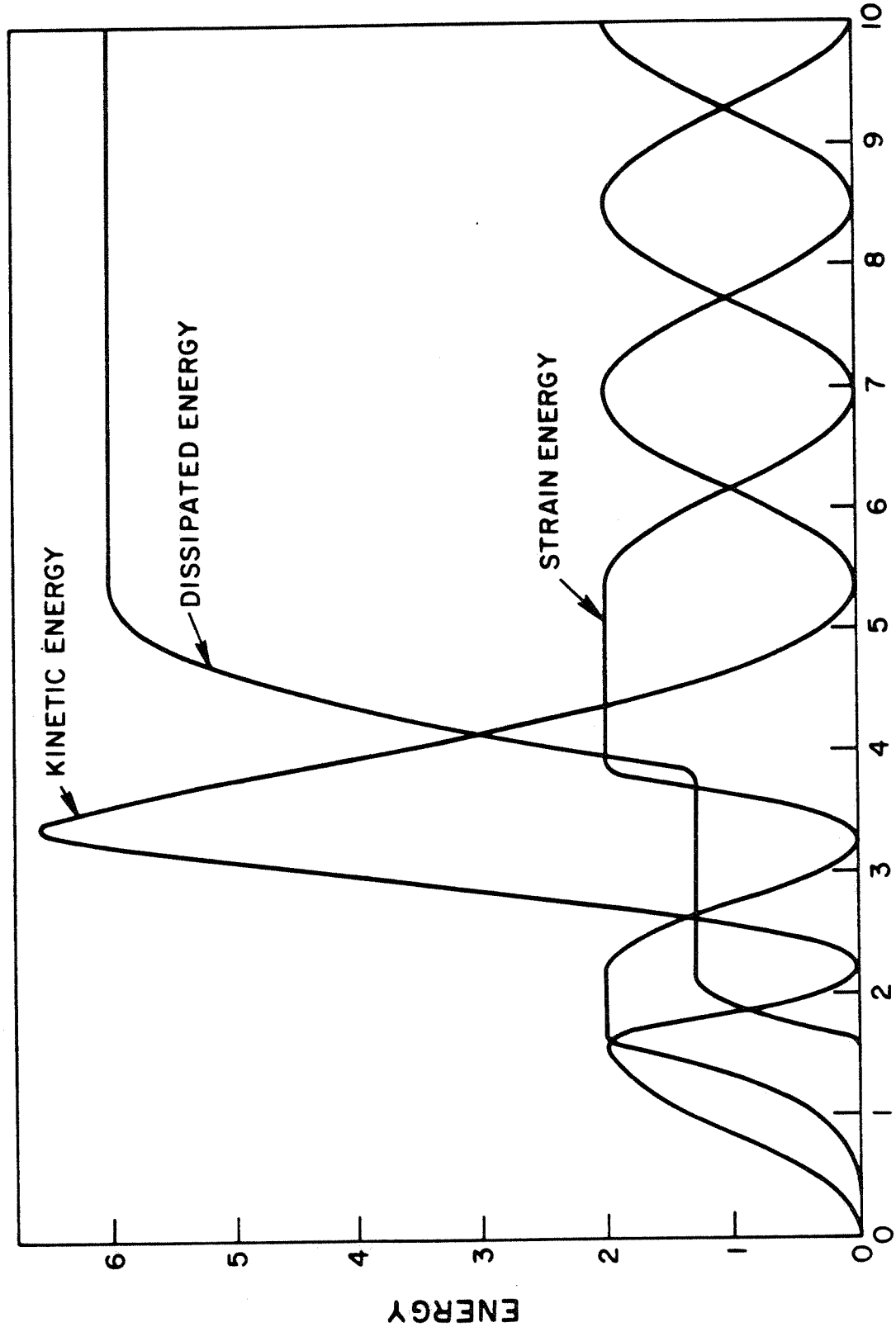

Fig. 14. Strain energy, kinetic energy and dissipated energy of the rigid block oscillator versus time.

elastically.

For the free oscillator conservation of energy requires that

$$E_D^n + E_K^n + U^n = E_o \quad , n = 0,1,2,\ldots,N, \qquad (5.1)$$

where E_D^n, E_K^n and U^n are the dissipated, kinetic and strain energies at time t_n, respectively, and E_o = const. (5.1) is satisfied by the discrete solution with $E_o = 8$. This can be seen from Figure 14, in which E_D^n, E_K^n and U^n are plotted versus time.

5.3 EFFECT OF INJECTION AND WITHDRAWAL IN A CRUDE FRACTURE MODEL WITH STICK-SLIP RATIO OF 0.98

Here let us consider a very crude model that we used to study the effect of injection and removal of fluid along a prestressed fault. The finite element mesh is shown in Figure 15. The boundary conditions are chosen such that the behavior of an infinitely long strip of rock along a planar fault is approximated. In the following we define the physical properties of the fluid, the solid material and the rock. The data is given in the units of pounds, feet, seconds.

Fluid: specific weight $\gamma = 62.4$; viscosity $\mu = 0.235\ 10^{-4}$; initial pressure $p_o = .3\ 10^5$.

Solid material: density $\rho = 5.12$; modulus of elasticity $E = 5.0\ 10^8$, Poisson ratio $\nu = 0.25$; initial state of stress $\sigma_{xx} = -2.0\ 10^5$, $\sigma_{yy} = -6.0\ 10^5$, $\sigma_{zz} = -2.0\ 10^5$, $\sigma_{xy} = -1.4\ 10^5$.

Fracture: initial tangent moduli $k_{no} = 10^8$, $k_{so} = 10^8$; initial state of stress $f_{no} = -1.7\ 10^5$, $f_{so} = -1.4\ 10^5$; cohesion $C = 0$; angle of friction $\phi = 40°$; stick-slip ratio $\alpha = 0.98$; initial aperture $d_o = 0.01$; average depth available for fluid flow $A = 100$.

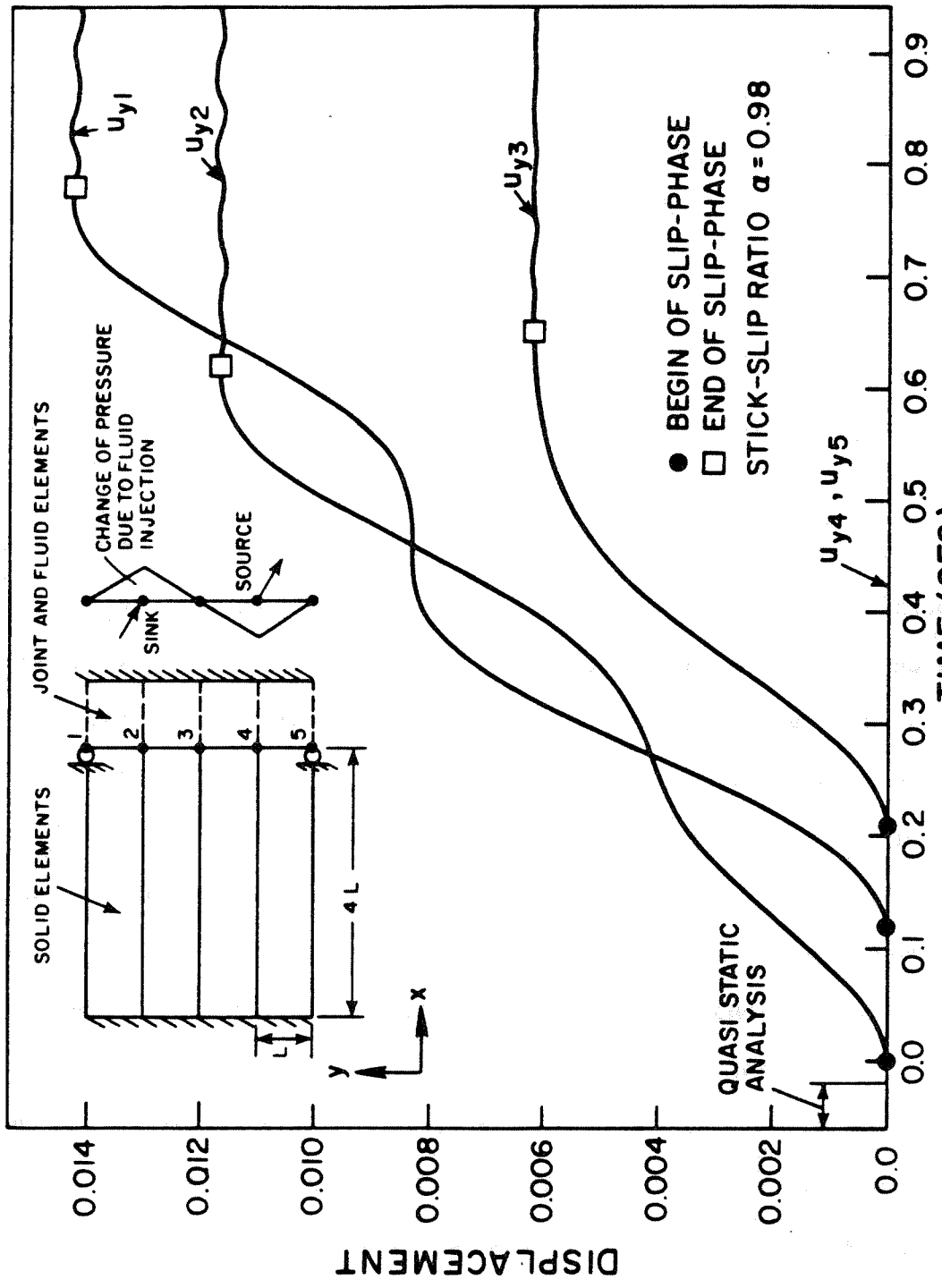

Fig. 15. General set-up of problem 3, and nodal displacements parallel to the fracture plane versus time.

The length of a joint element L = 1000, the time step size $\Delta t = 0.01$, and the convergence tolerances are $\varepsilon_s = 0.1$ and $\varepsilon_F = 0.001$.

Initially the system is at a state of static equilibrium with no fluid flow. As fluid is injected and removed in equal amounts at nodes 2 and 4, respectively, a pressure gradient along the flow path starts to build up, as indicated in Figure 15. It is assumed that the amount of injected fluid is increased very slowly, such that the response of the system can be determined by a quasi-static, steady-state analysis.

As the fluid pressure at node 2 builds up, the fracture at this point starts to open and the absolute magnitude of f_n decreases. Thus, as a consequence of (2.12), the associated shear peak strength f_{sy} decreases correspondingly. The quasi-static process is continued until f_{sy} has been reduced down to approximately the value of $|f_{so}|$, the initial shear stress. At this state the program switches to a dynamic mode of analysis. The amounts of injected and removed fluid are further increased until $f_{sy} \leq |f_{so}|$. At this point failure occurs, the residual strength is set equal to αf_{sy}, and the out-of-balance force $(f_{so} - \alpha f_{sy})$ starts to accelerate the rock masses into a shear motion in y-direction. The corresponding nodal displacements u_y, taken as functions of time, are plotted in Figure 15. The inertia forces which are related to the motion of node 2 lead to increased shear stresses and hence failure at the adjacent nodes 1 and 3. Eventually all three nodes 1 to 3 move into new permanently displaced equilibrium positions, as can be seen from Figure 15. Due to the locking effect of the reduced fluid pressure around node 4, nodes 4 and 5 do not fail in shear.

5.4 EFFECT OF INJECTION AND WITHDRAWAL IN A CRUDE FRACTURE MODEL WITH STICK-SLIP RATIO OF 0.99.

The problem of example 3 was solved with a somewhat finer mesh and a

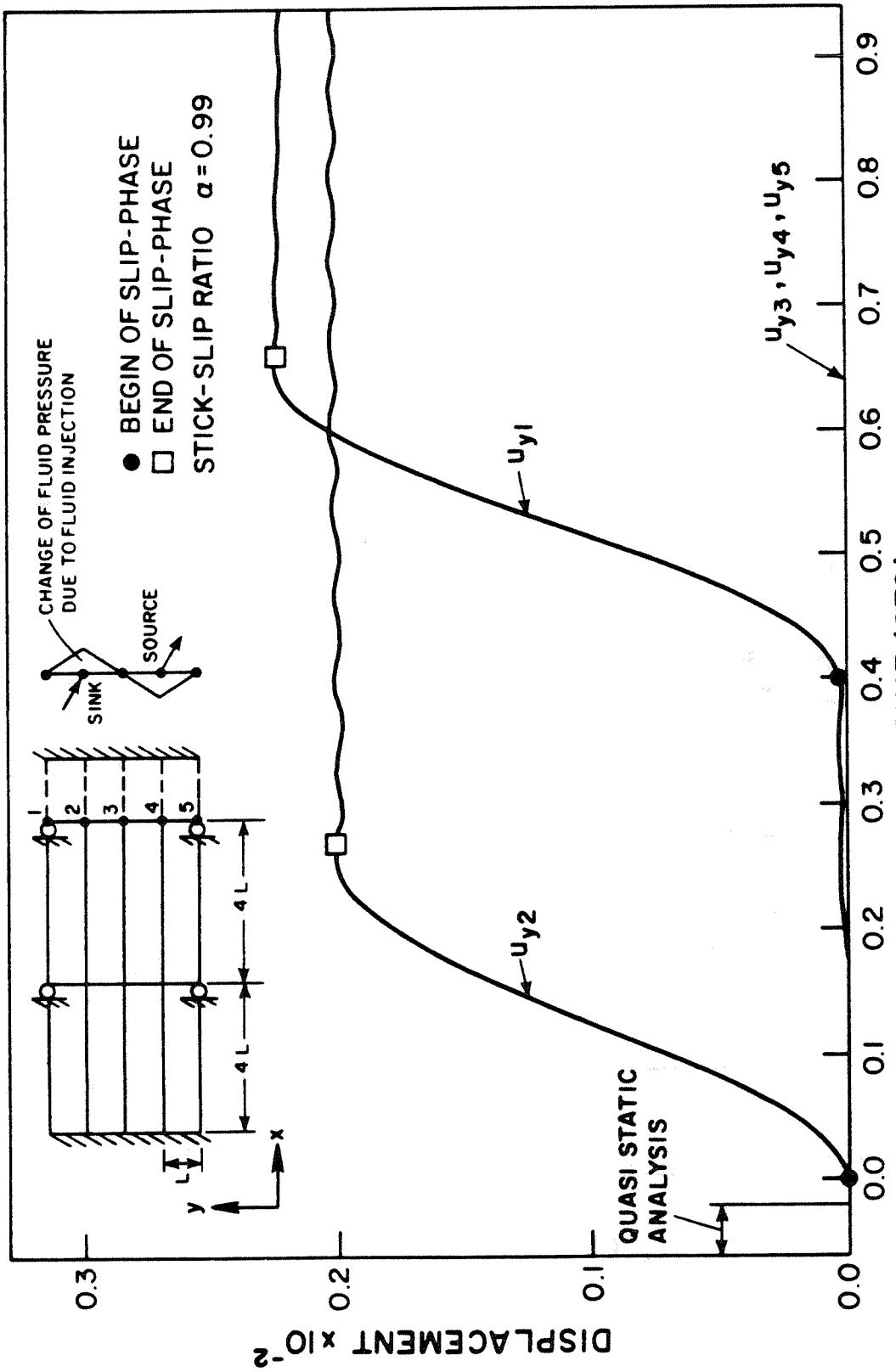

Fig. 16. General set-up of problem 4, and nodal displacements parallel to the fracture plane versus time.

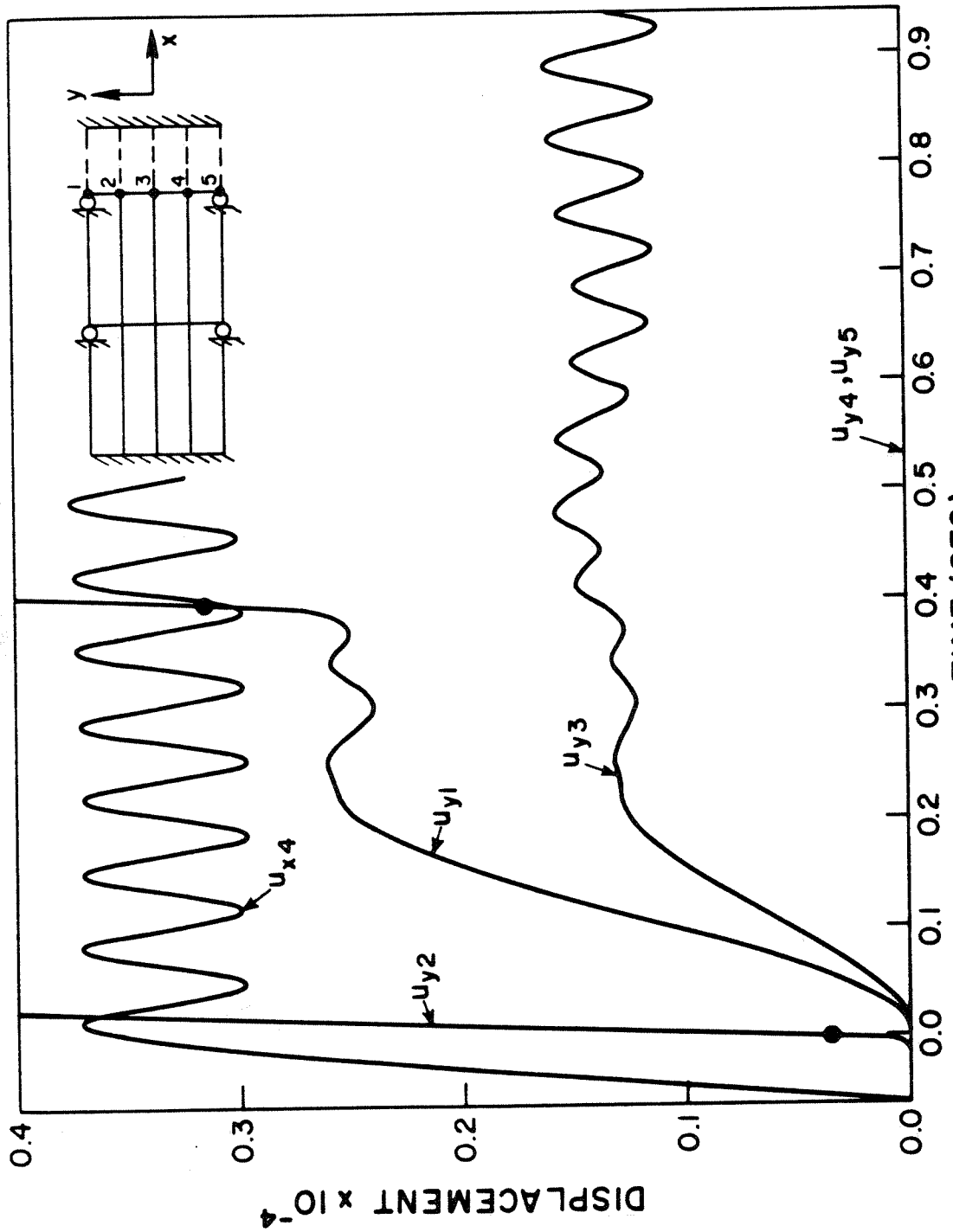

Fig. 17. Nodal displacements of fracture versus time.

stick-slip ratio $\alpha = 0.99$. The new mesh and the corresponding displacement histories $u_y(t)$ of nodes 1 and 2 are depicted in Figure 16. Figure 17 shows the displacement response histories of nodes 1, 2 and 3 in a larger scale. The final increase of pressure which was necessary to create failure at node 2 induced a vibration of nodes 2 and 4 in x-direction, as indicated in Figure 17. The motions of some points within the continuous rock are indicated in Figure 18, in which the response functions $u_y(t)$ of nodes 6, 7, 8 and 10 are plotted.

The original joint element, as introduced in [7], employes a one-point integration rule. It has been explained in Chapter 3, why this is inadequate in general: The one-point integration rule neglects the strain energy due to nonuniform deformation patterns. Hence, a joint element based on a two-point Gaussian integration rule was tested. However, this formula introduces coupling between the sections 1,4 and 2,3 of the joint element (see Figure 2), which, in turn, can cause the joint element to simulate friction and contact mechanisms in a physically incorrect way. For example, consider the displacement response histories of nodes 1 and 2 corresponding to the joint element with Gaussian integration, shown in Figure 19. The interaction between the degrees of freedom of adjacent nodes along the fault prevents the individual masses from being locked at the points of maximum displacement (i.e. zero velocity), and thus leads to physically meaningless results, as indicated in Figure 19.

5.5 EFFECT OF INJECTION AND WITHDRAWAL IN A CRUDE FRACTURE MODEL WITH STICK-SLIP RATIO OF 0.94.

In this example we consider a rigidly supported mass of rock, which is subdivided by a straight fracture into two equal parts. The finite element

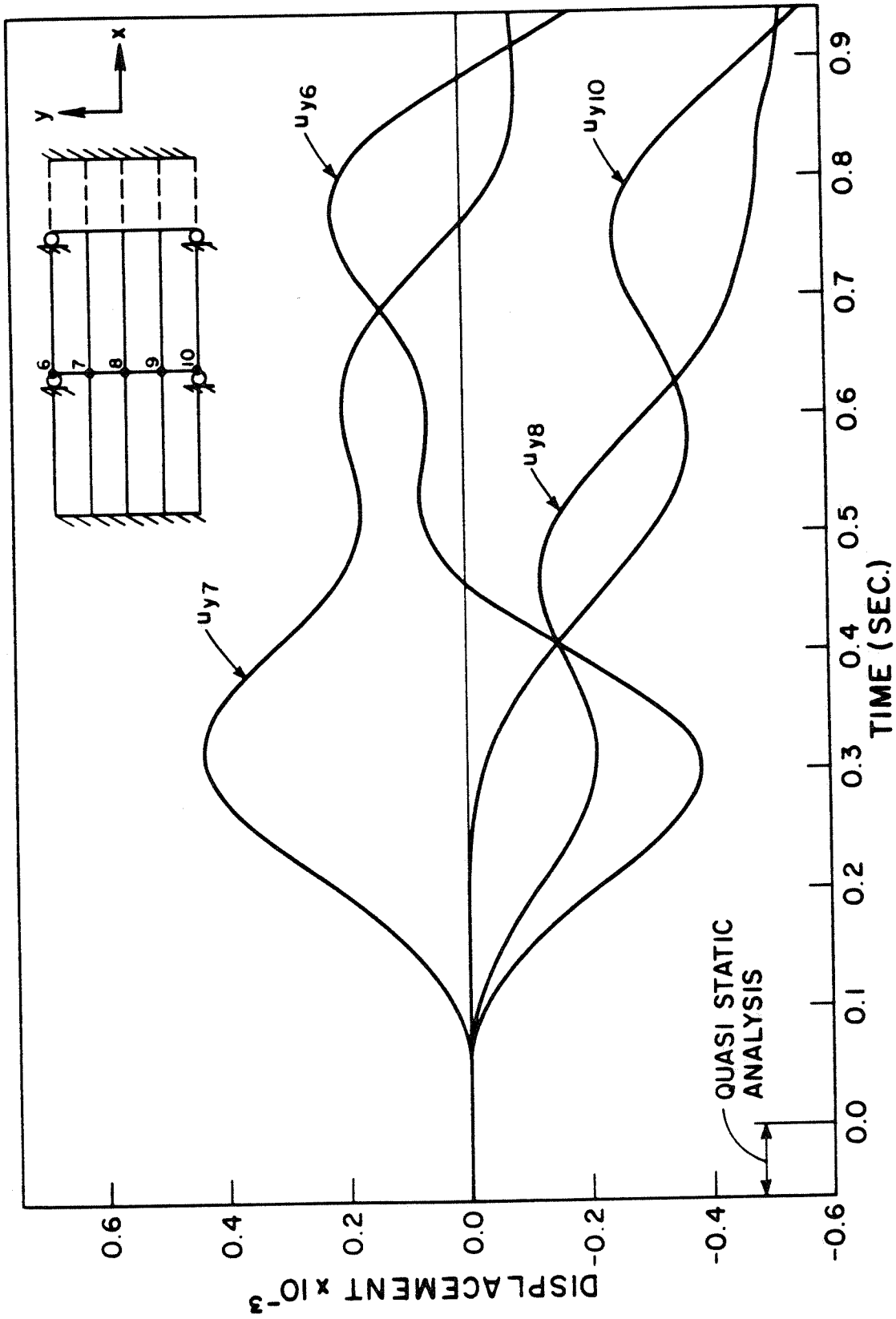

Fig. 18. Displacement histories of some points inside the elastic rock.

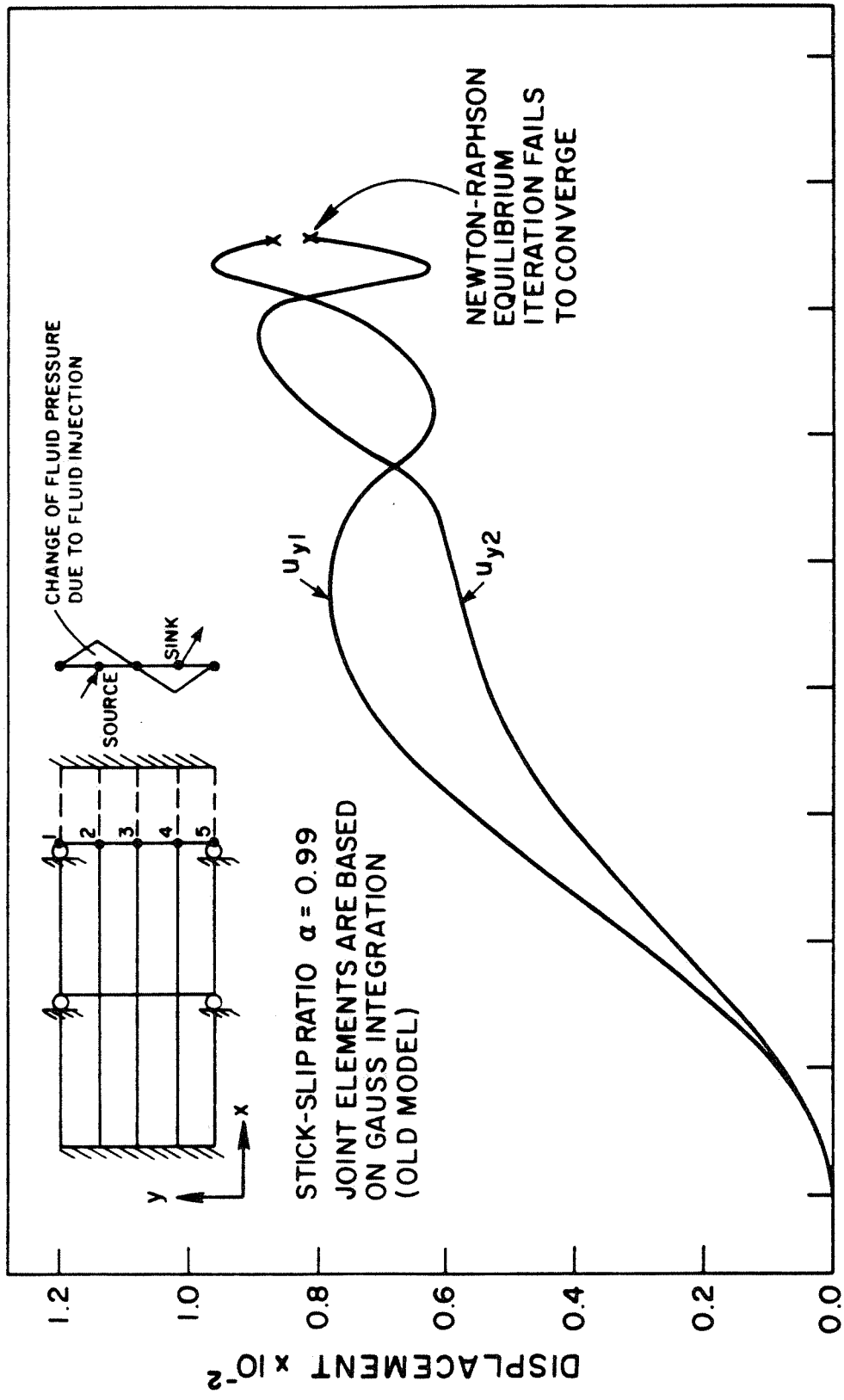

Fig. 19. Results generated by joint elements which are based on a two-point Gauss integration.

mesh and the steady-state fluid pressure profile in the fault are schematically indicated in Figure 20. The physical data are the same as for example 3, except that $\alpha = 0.94$, and the initial shear stress is assumed to be $\sigma_{xy} = -1.35\ 10^5$. In this case, compared to the previous two examples, a larger amount of water must be pumped into the fracture system in order to cause failure.

The artificial sources and sinks are equidistantly distributed along the fault, as indicated in Figure 20. In general, the fluid pressure profile in the fault depends on the distances between the artificial sources and sinks and on the amounts of fluid injected and removed at the various locations. The specific pressure distribution in the present case was created by pumping in at section 4,11 only two thirds of the total amount of fluid which is removed at sections 2,9 and 6,13.

Again, as in the previous two examples, the structure is initially in a prestressed state of static equilibrium. As the artificial sources and sinks are activated, a quasi-static process starts to redistribute the stresses, such that the peak shear strength (failure limit) around the center (nodes 4,11) is reduced, but around the artificial sources it is increased. As soon as an incipient state of instability is reached, a dynamic mode of analysis is employed to study the failure and the subsequent transient states of the system. In Figures 20 and 21 the displacement response histories of nodes 1 to 7 are shown. Only the three center nodes failed and thus have been permanently displaced. The fault did not fail in the lateral parts away from the center. This can be explained by the locking effects caused by fluid removal through the artificial sources.

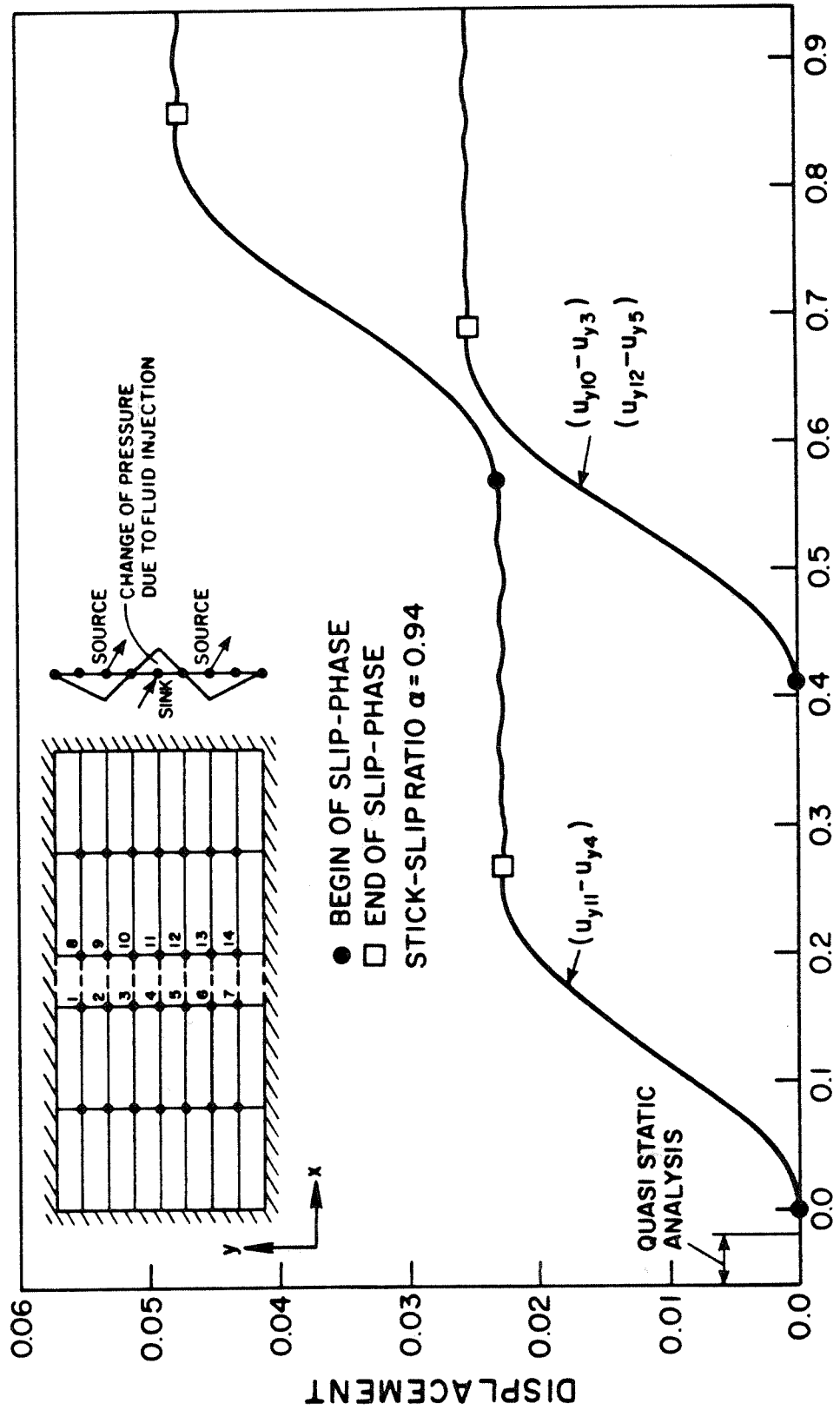

Fig. 20. Definition of problem 5, and displacement histories of some nodal points along the fault.

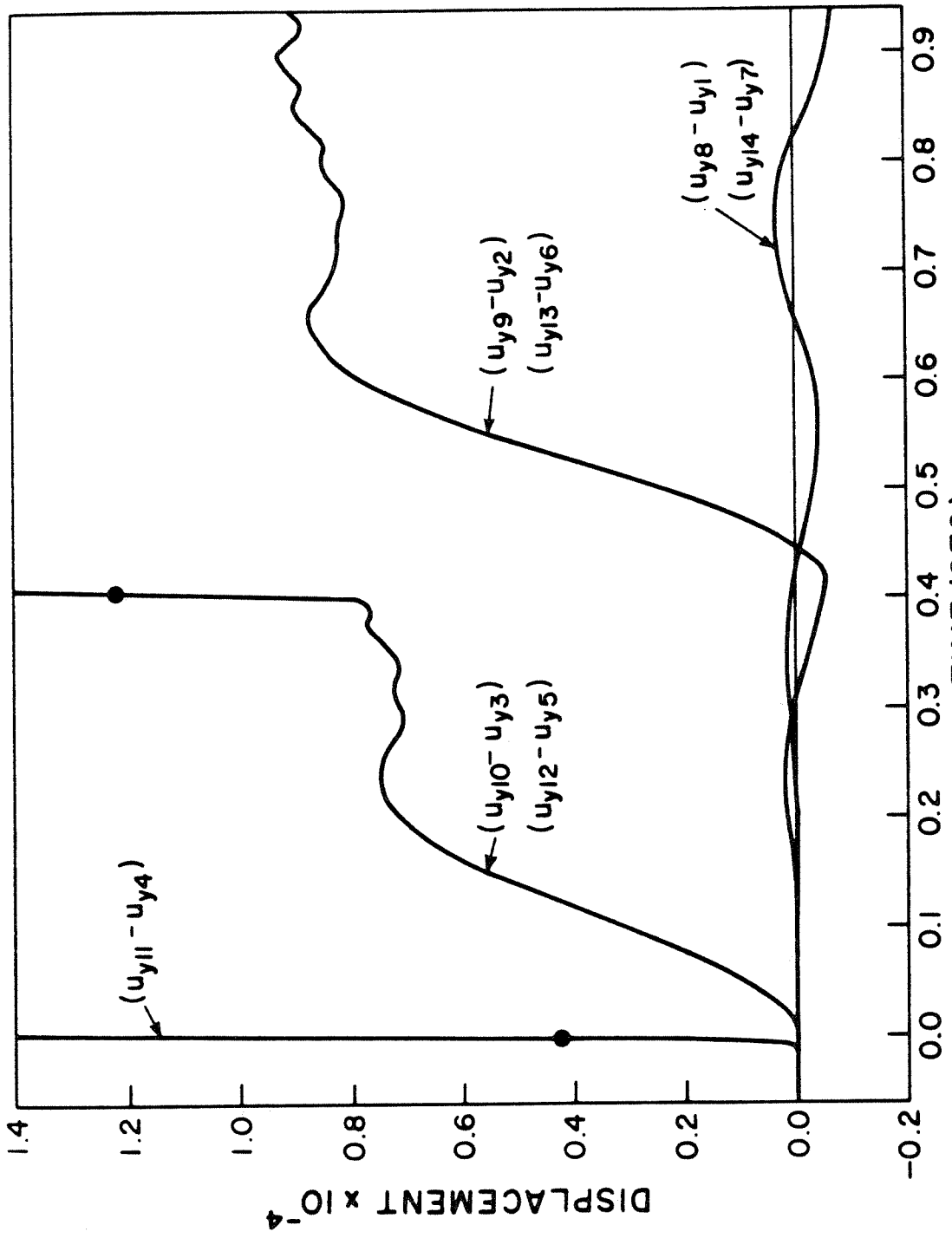

Fig. 21. Nodal displacements along the fault versus time.

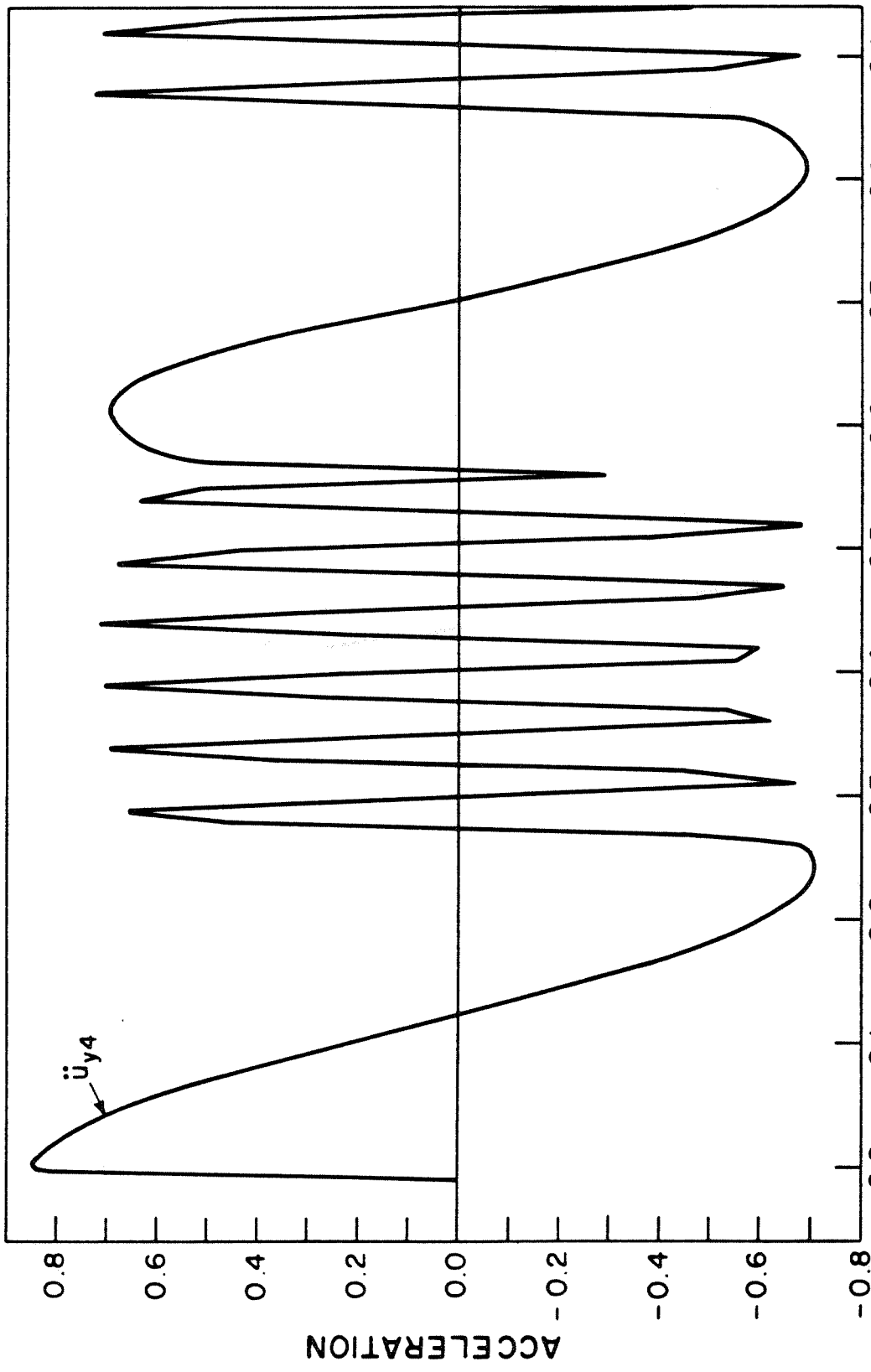

Fig. 22. Acceleration of node 4 in direction parallel to fault versus time.

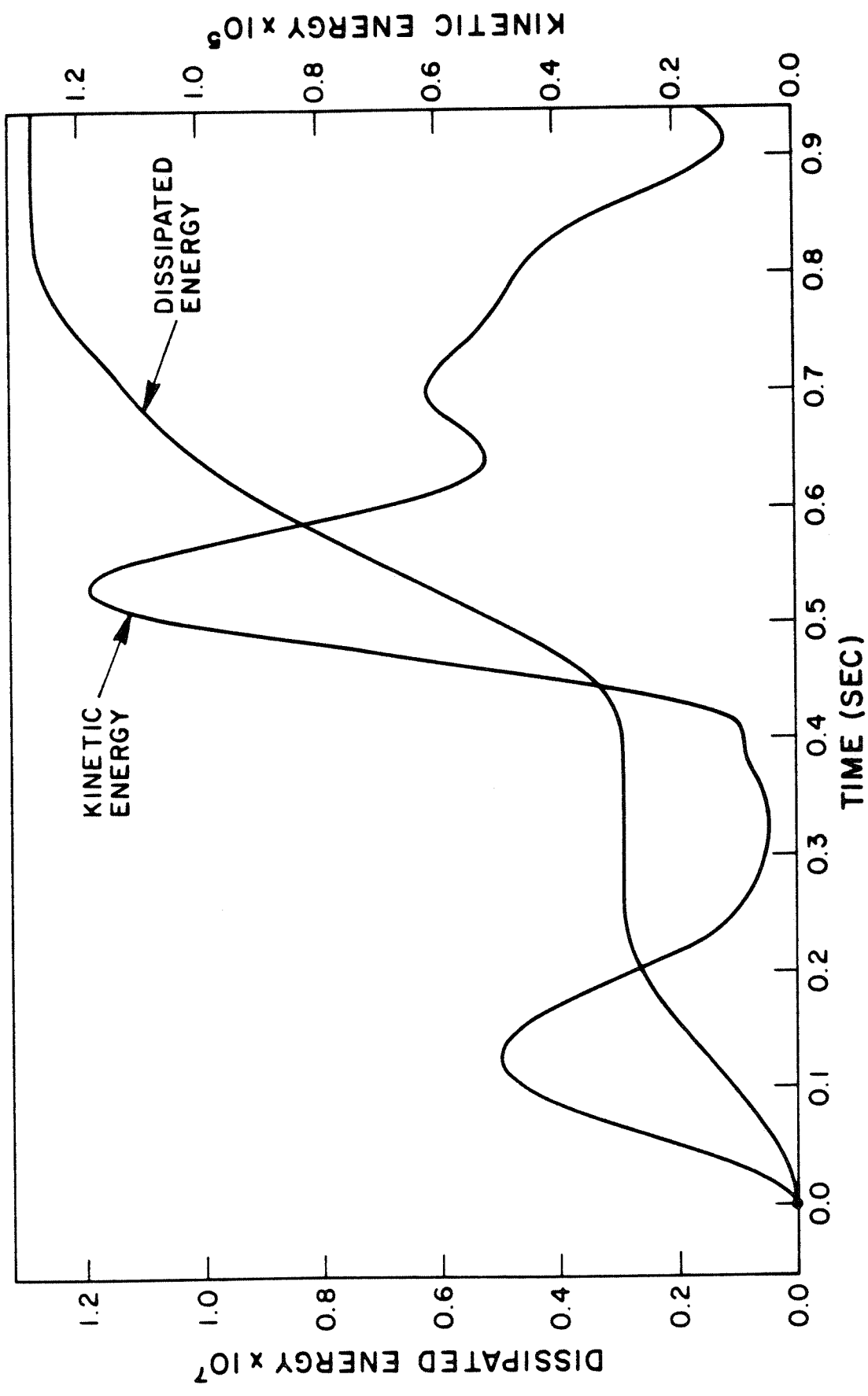

Fig. 23. Kinetic energy of the rock and energy dissipated during slip versus time for system of example 5.

The y-acceleration of nodal point 4 as function of time is plotted in Figure 22. The slip phases are clearly distinguished from the phases of linear elastic oscillations around the new positions of equilibrium indicated in Figure 20.

The energy dissipated during slip and the kinetic energy of the rock as functions of time are plotted in Figure 23. The change in strain energy of the system, denoted by ΔU^n can be computed from

$$E_D^n + E_K^n + \Delta U^n = E_{Ko} + \Delta U_o \quad , n = 0,1,2,\ldots,N, \quad (5.2)$$

where E_{Ko} is the kinetic energy and ΔU_o is the change in strain energy at the instant of failure. In the present case $E_{Ko} + \Delta U_o = -0.5\ 10^4$.

6. CONCLUSION

A mathematical model of fluid flow in nonstationary systems of deformable fractured rock has been developed. The model is based on a two-dimensional finite element formulation which incorporates inertia effects and accounts for the interaction between the fluid and the solid domains of the region considered. This enables one to predict the behavior of systems at an incipient state of instability when their state of stress is changed by injection and removal of fluid. The corresponding computer program allows idealized geological structures to be investigated under a large variety of conditions. The program determines the hydrodynamic states of the fluid and the displacement, strain and stress response histories of the rock masses during quasi-static and dynamic processes. Also the potential, kinetic and dissipated energies are computed as functions of space and time.

REFERENCES

1. J. H. Dietrich, C. B. Raleigh and J. D. Bredehoeft, "Earthquake Triggering by Fluid Injection at Rangely, Colorado", Proceedings Symposium of International Society for Rock Mechanics, Percolation through Fissured Rock, Stuttgart, Germany, September 18-19, 1972.

2. J. H. Dietrich, "A Deterministic Near-Field Source Model",Proceedings Fifth World Conference on Earthquake Engineering, Rome, Italy, June 25-29, 1973.

3. J. Handin, and C. B. Raleigh, "Manmade Earthquakes and Earthquake Control", Proceedings Symposium of International Society for Rock Mechanics, Percolation through Fissured Rock, Stuttgart, Germany, September 18-19, 1972.

4. W. Rodatz and W. Wittke, "Wechselwirkung Zwischen Deformation und Durchströmung in Klüftigen, Anisotropen Gebirgen", Proceedings Symposium of International Society for Rock Mechanics, Percolation through Fissured Rock, Stuttgart, September 18-19, 1972.

5. N. R. Morgenstern and H. Guther, "Seepage into an Excavation in a Medium Possessing Stress-Dependent Permeability", Proceedings Symposium of International Society for Rock Mechanics, Percolation through Fissured Rock, Stuttgart, September 18-19, 1972.

6. J. Noorishad, P. A. Witherspoon and T. L. Brekke, "A Method for Coupled Stress and Flow Analysis of Fractured Rock Masses", Geotechnical Engineering Report No. 71-6, University of California, Berkeley, 1971.

7. R. E. Goodman, R. L. Taylor and T. L. Brekke, "A Model for the Mechanics of Jointed Rock", J. Soil Mech. Found. Div., Proc. ASCE, SM3, pp. 637-659, 1968.

8. J. E. Gale, R. L. Taylor, P. A. Witherspoon and M. S. Ayatollahi, "Flow in Rocks with Deformable Fractures", Proc. Int. Symposium on Finite Element Methods in Flow Problems, Swansea, United Kingdom, 1974, UAH Press, The University of Alabama in Huntsville, 1974.

9. R. E. Goodman and J. Dubois, "Duplication of Dilatancy in Analysis of Jointed Rocks", J. Soil Mech. Found. Div., Proc. ASCE, SM4, pp. 399-422, 1972.

10. J. Ghaboussi, E. L. Wilson and J. Isenberg, "Finite Element for Rock Joints and Interfaces", J. Soil Mech. Found. Div., Proc. ASCE, SM10, pp. 833-848, 1973.

11. G. L. Goudreau and R. L. Taylor, "Evaluation of Numerical Integration Methods in Elastodynamics", Computer Meth. Appl. Mech. and Eng. 2, pp. 69-97, 1973.

12. O. C. Zienkiewicz, "The Finite Element Method in Engineering Science", McGraw-Hill, London, 1971.

13. G. Strang and G. J. Fix, "An Analysis of the Finite Element Method", Prentice Hall, Englewood Cliffs, New Jersey, 1973.

14. H. M. Hilber, T. J. R. Hughes, and R. L. Taylor, "Improved Numerical Dissipation for Time Integration Algorithms in Structural Dynamics", to appear in J. of Earthquake Engineering and Structural Dynamics.